

NACA RM L53G02

TECH LIBRARY KAFB, NM
0144320

NACA

RESEARCH MEMORANDUM

INVESTIGATION OF AN AXIAL-FLOW COMPRESSOR ROTOR HAVING

NACA HIGH-SPEED BLADE SECTIONS (A_{2I8b} SERIES)

AT MEAN RADIUS RELATIVE INLET

MACH NUMBERS UP TO 1.13

By Melvyn Savage, John R. Erwin, and Robert P. Whitley

Langley Aeronautical Laboratory
Langley Field, Va.

CLASSIFIED DOCUMENT

NATIONAL ADVISORY COMMITTEE
FOR AERONAUTICS

WASHINGTON

November 30, 1955



NATIONAL ADVISORY COMMITTEE FOR AERONAUTICS

RESEARCH MEMORANDUM

INVESTIGATION OF AN AXIAL-FLOW COMPRESSOR ROTOR HAVING

NACA HIGH-SPEED BLADE SECTIONS ($A_{2I_{80}}$ SERIES)

AT MEAN RADIUS RELATIVE INLET

MACH NUMBERS UP TO 1.13

By Melvyn Savage, John R. Erwin, and Robert P. Whitley

SUMMARY

A high-pressure-ratio, axial-flow compressor rotor designed to operate efficiently at high speeds was investigated at air equivalent tip speeds from 674 to 1185 ft/sec. The tests for tip speeds above 848 ft/sec were made by using a Freon-12 atmosphere because of power and speed limitations. The compressor blading was the NACA $A_{2I_{80}}$ -series blades designed to give efficient performance at high inlet Mach numbers. The investigation covered a range of relative inlet Mach numbers at the mean radius of the rotor from 0.63 to 1.13.

The use of low-speed cascade data for determining design angles of attack was quite effective in that peak efficiency and design angle-of-attack efficiency were coincident for inlet Mach numbers up to 0.87. Above 0.87, while design angle-of-attack efficiency decreased rapidly, peak efficiency gradually decreased from 0.96 to 0.90 at a Mach number of 0.96 where total pressure ratio was 1.555. The shift in peak efficiency to higher than design angles of attack for mean radius inlet Mach numbers above 0.87 may have resulted because (1) the severity of the operating conditions for the blade lower surface increased as inlet Mach number approached the transonic range, and (2) the amount of improvement in lower surface performance obtained by increasing the angle of attack 4° above design in the transonic Mach number range more than compensated for any associated decline in upper surface performance.

Two-dimensional low-speed cascade data agreed very well with the high-speed rotor-corrected turning-angle data in the angle-of-attack region from 12° to 14° . At 10.6° , the design angle of attack obtained from low-speed cascade data, the cascade predicted turning angles were about 2° too high.

~~CONFIDENTIAL~~

11-3-19

For an inlet air angle of 60° , measured turning angles at the mean radius section were found to be independent of Reynolds numbers over the test range from 120,000 to 920,000 at a mean radius Mach number of 0.61. At this inlet air angle, the effect of inlet Mach number on turning angle was negligible from Mach numbers of 0.10 to 0.85. From 0.85 to 1.10 the turning angle decreased approximately 1.3° .

INTRODUCTION

The design of efficient, high-pressure-ratio, high-flow blade rows for axial-flow compressors is desirable from size, weight, and production considerations. Higher flows are needed to increase engine thrust without increasing engine frontal area. A reduction in the number of stages for a given over-all pressure ratio may improve compressor operating range by reducing the stage matching difficulties encountered with large numbers of stages. Increases in both weight flow and stage pressure ratio are limited by the maximum rotor relative inlet Mach numbers that can be used without an appreciable reduction in efficiency. Rotor and stage tests of highly loaded blade rows operating at high subsonic inlet Mach numbers were reported in references 1, 2, and 3. Rotor efficiency monotonically decreased from 95 to 84 percent when the mean radius rotor inlet Mach number reached 0.82 in reference 1, and from 93 to 84 percent when the Mach number reached 0.84 in reference 3. An extension of the useable inlet Mach numbers is necessary if substantial improvements in engine performance can be realized from improved axial-flow compressor design.

The compressor blades used in the above-mentioned references were NACA 65-series blades having $a = 1.0$ mean lines. In compressor cascades, $a = 1.0$ mean lines carry more of the loading in the forward half of the blades than in the rearward half. In order to increase the maximum inlet Mach numbers without excessive losses, a new series of compressor blades was developed (ref. 4) utilizing a mean-line shape which shifted the loading toward the rear portion of the blade, in conjunction with the NACA 65-series thickness distribution. Reference 4 presents the low-speed cascade tests for these blades, called NACA A_2I_{8b} -series blades, over a range of inlet air angles, solidities, and cambers. A complete description of the blade-series-designation system is presented in reference 5.

A rotor having A_2I_{8b} -series blades was designed and constructed at the Langley Aeronautical Laboratory to determine whether the rearward shift in blade loading would raise the permissible design inlet Mach number level and hence, the design pressure ratio and weight-flow level. Tests were made at equivalent tip speeds ranging from 674 to 1185 ft/sec over a range of weight flows. A schlieren system was developed by Mr. James R. Sterrett, of the Langley Laboratory, in order to permit

observation of the flow upstream of the rotor. Motion pictures utilizing this schlieren system were taken for several different throttle settings and rotational speeds.

The Langley Aeronautical Laboratory first noted that efficient rotor performance at transonic rotor inlet Mach numbers was possible using the A₂I₈₀ series blades in February 1951.

SYMBOLS

A	blade passage area, sq ft
c	blade chord, in.
C _L	lift coefficient
c _p	specific heat at constant pressure, ft-lb/slug/°F
M	Mach number, ratio of flow velocity to the velocity of sound
n	rotor speed, rps
p	static pressure, lb/sq ft
p ₀	stagnation pressure, lb/sq ft
q	dynamic pressure, $\frac{\gamma}{2} \rho M^2$, lb/sq ft
r	radial position measured from axis of rotor
R	gas constant (for pure Freon-12, 411.5; for air, 1716 ft-lb/slug/°F)
R _n	Reynolds number based on mean radius blade chord
T ₀	stagnation temperature, °R
ΔT ₀	isentropic change in stagnation temperature across the rotor, °F
U	rotational velocity, 2πrn, ft/sec
V	velocity of fluid, ft/sec

~~CONFIDENTIAL~~

ΔV_u	change in tangential velocity across rotor, ft/sec
W	weight flow, lb/sec
X	blade section abscissa, in.
Y	blade section ordinate, in.
α	angle of attack, angle between blade chord and flow direction, deg
β	angle between flow direction and the rotor axis, deg
γ	ratio of specific heats (1.40 for air and 1.125 for pure Freon-12)
δ	ratio of actual inlet stagnation pressure to standard sea-level pressure, $p_o/2116$
η	rotor mass flow weighted adiabatic efficiency
θ	ratio of actual inlet stagnation temperature to standard sea-level temperature, $T_o/518.4$
ρ	density, slugs/cu ft
σ	solidity, ratio of blade chord to blade spacing
ϕ	turning angle in rotor coordinates, deg

Subscripts:

a	axial
av	average
c	equivalent velocity vectors based on constant axial velocity diagram
d	design
h	hub
L	blade section lower surface
m	mean radius
r	rotor coordinates
s	stationary coordinates

t tip
T minimum area section in blade passage
U blade section upper surface
air air data
Freon Freon data
1 rotor entrance
2 rotor exit

APPARATUS AND PROCEDURE

Rotor Design

The high-pressure-ratio compressor rotor used for this investigation is shown in figure 1. NACA A₂I_{8b}-series compressor blades (ref. 5) were used at a constant solidity of 1.0 with maximum blade thickness ranging from 10 percent at the hub to 8 percent at the tip. The rotor hub-tip radius ratio was 0.75 and the tip diameter was 16.0 inches. Blade section coordinates are presented in table I. Tip clearance was approximately 0.030 inch. With the cascade data available at the time this rotor was designed, which consisted of tests at an inlet air angle of 60° and a solidity of 1.0, design angles of attack were chosen from the blade pressure distributions to insure no velocity peaks on the upper and lower blade surfaces. These values should represent the angle of attack with the highest critical Mach number.

The rotor was designed for constant power input from hub to tip. At the design tip speed of 808 ft/sec a total pressure ratio of 1.258 was anticipated for the assumed design efficiency of 0.92. The annulus was constant across the rotor. The design exit axial-velocity was determined from continuity considerations using an exit effective area equal to 94 percent of the actual area to account for wall boundary-layer build-up. The velocity diagrams at the hub, mean; and tip radius sections are presented in figure 2. The use of two-dimensional cascade data for design purposes necessitated the use of an equivalent constant axial-velocity diagram based on the mean of the rotor inlet and exit axial velocities (ref. 6). A summary of the blade design data is presented in the following table. All angles are in terms of the equivalent velocity diagrams.

~~CONFIDENTIAL~~~~CONFIDENTIAL~~

The following table presents pertinent design parameters for the rotor:

	Hub	Mean	Tip
Radius ratio, r/r_t . .	0.750	0.875	1.000
Turning angle, deg . .	26.7	17.2	11.6
Angle of attack, deg .	15.0	10.6	9.0
Relative inlet			
Mach number	0.697	0.771	0.850
Inlet air angle, deg .	53.7	57.8	61.1
Chord, in.	1.885	2.199	2.513
Solidity	1.00	1.00	1.00
Blade section	65-(18.5A ₂ I _{8b})10	65-(11.3A ₂ I _{8b})09	65-(7.3A ₂ I _{8b})08
$p_2 - p_1$	0.60	0.54	0.48
q_1			
Blade loading parameter, σC_L . . .	0.79	0.64	0.53

Test Apparatus and Instrumentation

A schematic drawing of the compressor test rig is presented in figure 3. This test rig has been described in reference 7. Four fixed total-pressure tubes were installed in the settling chamber downstream of the screens at 90° intervals. A radial survey of total and static pressure and flow direction made upstream of the rotor indicated that the flow into the rotor was uniform except for a very thin boundary layer on the walls. Wall static-pressure taps located approximately 1 inch upstream of the rotor on the inner and outer walls were used in conjunction with the settling chamber stagnation pressure and temperature to obtain the upstream weight flow. For all operating conditions 15 point radial surveys of total and static pressure and flow direction were taken approximately $4\frac{1}{2}$ inches downstream of the rotor using a combination probe of the type shown in reference 6. There were inner and outer wall static taps downstream of the rotor at this axial station.

All pressures were recorded simultaneously by photographing a mercury filled manometer board. The upstream static pressure and stagnation pressure leads were also connected to a water-filled U-tube to improve accuracy in determining the weight flow. The rotor speed was measured by a calibrated tachometer with an accuracy of ± 1.5 revolutions per minute.

~~CONFIDENTIAL~~

Total temperature measurements were made in stagnation regions before and after the rotor by five thermocouples at each station. In addition, calibrated aircraft-type electrical resistance thermometers were installed to supplement the thermocouple readings. A rake of four shielded thermocouples was located 1 inch downstream of the rotor.

The motor and step-up gear train were mounted on ball-bearings and the reaction torque was determined by using a pneumatic pressure cell. The tare torque was determined by using a dummy hub and making tests over a wide range of rotational speeds and pressures.

In those runs conducted in a Freon atmosphere, the velocity of sound in the Freon-air mixture was measured by an instrument similar to that described in reference 8 in which a calibrated Helmholtz resonator was used to measure the speed of sound.

The schlieren system set up to permit flow observation upstream of the rotor utilized a 1- by 1.1-inch mirror inserted in the inner casing approximately 0.21 inch upstream of the rotor leading edge. The shock location and strength will differ from hub to tip, and, therefore, the schlieren system yields only a qualitative picture of conditions in this region. A schematic drawing of the schlieren apparatus, which passed parallel light through the disturbance field twice, is shown in figure 4. In order to stop the motion of any disturbance in the flow field, a stroboscopic mercury-arc light with a time duration of approximately 4 microseconds was flashed for each complete rotor revolution. A signal from an electromagnetic "pick-up" located near the rotor shaft went to an electronic amplifier which triggered the mercury-arc light. A variable-speed camera was adjusted so that its shutter would be completely open for every third flash of the light, and completely closed for the other two flashes. This was done to make possible the use of a low-speed camera. An electrical contact was placed on the camera to indicate the midposition of open shutter. The resulting signal, along with an electrical signal generated every time the light flashed, was impressed upon an oscilloscope. The operator of the camera could watch the pattern on the oscilloscope, and by varying the voltage to the camera motor, could synchronize the open position of the camera shutter with the light flashes. The resulting film could thus be used as a movie or as individual frame photographs.

Tests

The lower tip-speed tests (tip speeds from 674 to 848 ft/sec) were made in air. The higher tip-speed tests (air equivalent tip speeds ranging from 926 to 1185 ft/sec) were made in Freon-12 because of speed and power limitations of the drive motor. At each tip speed the weight flow was varied from near stall to that associated with wide open throttle setting. Stall is herein defined as rotor surge characterized by flow fluctuation.

Detailed traverses of static and total pressure and flow direction were made at each weight flow. The absolute stagnation pressure in the settling chamber was maintained by an automatic pressure control at approximately 13 inches of mercury for the air runs and varied from 9 to 12.5 inches of mercury for the Freon-12 tests.

Using the schlieren and camera system previously described, motion pictures of flow conditions upstream of the rotor were taken while the rotational speed was varied at constant throttle setting and while the throttle setting was varied at constant speed.

With the downstream survey instrument at the mean radius, tests were conducted in both Freon and air to determine the effect of rotor inlet Mach number on turning angle at the mean radius for a particular inlet-air-angle (angle-of-attack) condition. The mean radius blade section was a 65-(11.3A₂I_{8b})09 set at a value of $\beta - \alpha$ of 47.2° . Several speeds were run, and at each speed the throttle setting was adjusted so that the corrected mean radius inlet air direction was set at 60° from the axial direction ($\beta_d = 57.8^\circ$). The corrected inlet air angles and corrected turning angles were obtained from the equivalent constant axial velocity diagrams obtained from the measured results. Corresponding to this inlet air angle of 60° , the corrected angle of attack is 12.8° . The test Reynolds numbers based on mean radius chord ranged from 3.0×10^5 to 3.4×10^5 for the air tests and from 9.4×10^5 to 10.7×10^5 for the Freon tests.

Tests were also made to determine the effect of Reynolds number on mean radius turning angle at constant mean radius inlet Mach number. For the air tests, the tip speed was set at 672 ft/sec and Reynolds numbers ranging from 1.2×10^5 to 5.1×10^5 were obtained by varying the system pressure (M_m was equal to 0.61). At each system pressure setting, the throttle was adjusted to maintain the corrected inlet air angle of 60° . Similar tests were run in Freon at an air equivalent tip speed of 672 ft/sec. For these tests, Reynolds numbers ranged from 3.2×10^5 to 9.2×10^5 .

METHODS OF DATA REDUCTION

Weight Flow

The agreement between weight flows measured upstream and downstream of the rotor was within ± 2.5 percent for the major part of the air tests and within ± 3.6 percent for the major part of the Freon tests. For the other air tests, which corresponded to the highest Mach numbers run in

air, the agreement was within ± 3.0 . For the other Freon tests, the agreement was within ± 4.5 percent. The largest discrepancy between upstream and downstream weight flows invariably occurred at the lowest weight flow tested for each rotational speed (very close to stall).

The weight flows presented in this report were those obtained from measurements upstream of the rotor since the downstream instruments are in a velocity field which varied rapidly in magnitude and direction and since an accurate calibration for the static-pressure survey probe was not available for Mach numbers above 0.45.

Over-All Total-Pressure Ratio

Over-all total-pressure ratios presented in this paper were obtained by a mass-weighted average of the isentropic power input obtained from the survey total-pressure measurements. The following equation was used with the integrations being done mechanically:

$$\frac{p_{o2}}{p_{o1}} = \left[1 + \frac{\int_{r_h}^{r_t} (\Delta T_o) \rho_2 V_{a2} d(r^2)}{T_{o1} \int_{r_h}^{r_t} \rho_2 V_{a2} d(r^2)} \right]^{\frac{\gamma}{\gamma-1}}$$

(ΔT_o) is the isentropic total temperature rise obtained from total-pressure measurements.

Conversion of Freon Test Data to Air Equivalent Test Data

The data obtained in Freon were converted to equivalent air conditions by equating inlet Mach numbers relative to the rotor at the mean radius. Then for the same stagnation conditions and no prerotation of the flow, from reference 7, the air equivalent rotational speed is given by

$$(U_{air})^2 = \left[\frac{\gamma R}{2 + (\gamma - 1) M_a^2} \right]_{air} \left[\frac{2 + (\gamma - 1) M_a^2}{\gamma R} \right]_{Freon} (U_{Freon})^2$$

The air equivalent weight flow is given by:

$$W_{\text{air}} = \left[\left(\frac{\gamma}{RT} \right)_{\text{air}} \left(\frac{RT}{\gamma} \right)_{\text{Freon}} \right]^{1/2} \left(\frac{p_{\text{air}}}{p_{\text{Freon}}} \right) W_{\text{Freon}}$$

In order to obtain the equivalent total-pressure ratio in air, the efficiency was assumed to be the same as the efficiency determined in the Freon test. This assumption, while probably not exact, is valid since the ratio of the static-pressure rise across a rotor to the inlet dynamic pressure $\Delta p/q$ is practically the same for a Freon test and its air equivalent. The Freon mass-weighted power input was obtained from the Freon efficiency and the Freon mass-weighted total-pressure ratio. The air equivalent mass-weighted power input was obtained by assuming that the rotor velocity diagram is similar for either fluid; that is, ΔV_u increases from Freon to air by the same ratio as the rotational speeds. This assumption is valid since the density ratio across the rotor is approximately the same for a Freon test and its air equivalent. By applying the Freon test efficiency to the air equivalent power input, the over-all air-equivalent total-pressure ratio was obtained. Check tests made at the same equivalent tip speed in air and Freon confirmed this method of obtaining air-equivalent total-pressure ratio.

Efficiency

The adiabatic rotor efficiencies based on momentum considerations were obtained from the following equation:

$$\eta = \frac{\int_{r_h}^{r_t} c_p (\Delta T_o) \rho_2 V_{a2} d(r^2)}{\int_{r_h}^{r_t} U \Delta V_{u2} \rho_2 V_{a2} d(r^2)}$$

Rotor efficiencies for the air tests were also determined by utilizing the measured total temperature rise to determine the actual power absorbed. Both methods of efficiency calculation required mechanical integrations of the 15-point traverses taken for each test condition. The agreement between the efficiencies obtained by both methods was within ± 3 percent. This agreement is within the temperature measuring accuracy of $\pm 0.75^\circ$ for total temperature rises from 25° F to 54° F. For the air tests, the efficiencies presented in the report were those

obtained from momentum considerations. They are the more conservative values of efficiency since they were generally lower than those obtained from temperature measurements.

Rotor efficiencies for the Freon tests were determined from a consideration of momentum change as described above and also a measurement of rotor reaction torque to obtain the actual power absorbed. The agreement between the efficiencies obtained by these methods is within ± 1.0 percent except for two of the 20 Freon tests where the agreement was within ± 1.8 percent. The efficiency obtained from temperature measurements was not considered to be accurate enough for the Freon tests because of the low total temperature rises (20° to 35°). For the Freon tests as well as the previously mentioned air tests, the efficiencies presented in this report were those based on momentum change. The efficiencies obtained from torque measurements were randomly scattered both above and below those presented.

RESULTS AND DISCUSSION

Over-All Total-Pressure Ratio and Adiabatic Efficiency

The over-all rotor total-pressure ratio plotted against corrected air weight flow $W\sqrt{\theta}/\delta$ at various corrected tip speeds $U_t/\sqrt{\theta}$ is presented in figure 5. The Freon test data presented in figure 5 have been corrected to equivalent air tests by the methods previously discussed in this report.

The dashed curves in figure 5 indicate the flow conditions for constant values of angle of attack, expressed as the difference between actual and design angle of attack at the mean radius. For the computation of the dashed curves, angles of attack are measured from the inlet flow direction. On this basis, design angle of attack at the mean radius is 9.4° while on an equivalent velocity diagram basis it is 10.6° . At the design point, a slightly higher pressure ratio was obtained than anticipated. This higher pressure ratio resulted mainly because the rotor efficiency obtained was 96 percent instead of the value of 92 percent assumed for design purposes.

The weight-flow operating range of this transonic rotor at low and moderate tip speeds is equivalent to that of typical subsonic rotors. Operating range is slightly reduced at the high tip speeds. Hence, from weight-flow operating range considerations, the matching problems involved in staging transonic blade rows should not be appreciably worse than those for subsonic blade rows. The surge line appeared to shift to somewhat higher weight flows for the Freon tests. A spot check was made

at $\frac{U_t}{\sqrt{\theta}} = 825$ ft/sec to determine the surge point for an air and Freon test at the same corrected tip speed. The surge point for the Freon test was found to occur at an air-equivalent weight flow approximately 5 percent greater than the actual air test. Hence, actual air tests at the higher tip speeds would probably have resulted in a smooth continuous surge curve.

Figure 6 presents the rotor performance data for the Freon tests. The total-pressure ratio, weight flow, and tip speed are Freon test values corrected to standard inlet conditions ($p_o = 2116$ lb/ft² and $T_o = 518.4^\circ$ R). The air equivalent values of pressure ratio, weight flow, and tip speed for these tests have been indicated in figure 5.

Figure 7 presents the adiabatic efficiencies plotted against air equivalent weight flows at constant tip speeds with both weight flow and tip speed corrected to standard sea-level conditions. The weight flows corresponding to design angle of attack at the mean radius are indicated by a short vertical dash for each tip-speed test. At $U_t/\sqrt{\theta}$ equal to 1088 ft/sec and above, the maximum weight flows obtainable were below the values corresponding to design angle of attack due to pressure losses in the radiators, valves, and screens in the test circuit. The weight flow corresponding to design angle of attack is in good agreement with that for peak efficiency at and below design speed ($\frac{U_t}{\sqrt{\theta}} = 808$ ft/sec).

As tip speed was increased above design, the weight flow for peak efficiency corresponded to higher-than-design angles of attack. Hence, the previously described method of determining the high-speed design angles of attack at which low-speed cascade test pressure distributions had no peaks was quite satisfactory at the low and moderate Mach numbers. It should be noted that the efficiency curves are quite flat at weight flows corresponding to design angle of attack and 4° above design in the low and moderate Mach number range. However, at the high Mach numbers where large regions of supersonic flow must occur, the problems involved in efficiently diffusing the flow which has these supersonic regions become of paramount importance and it is not surprising that the angles of attack selected from low-speed tests as described previously do not coincide with those at peak efficiency.

Figure 8 indicates the Mach number distribution from hub to tip at the various tip speeds. The dashed curves correspond to peak efficiency and the solid curves correspond to the design angle of attack. Since

design angle-of-attack weight flows were not obtained at $U_t/\sqrt{\theta}$ of 1088, 1125, and 1185 ft/sec, no solid curves were drawn at these speeds. As the tip speed was increased, the differences between the Mach numbers relative to the blades at peak efficiency and those at design angle of attack increased. This increase resulted from a steady shift in peak efficiency to weight flows corresponding to higher than design angles of attack with increasing tip speed.

Figure 9 summarizes the rotor performance characteristics corrected to air equivalent pressure ratios, weight flows, and rotational speeds. Efficiency contours are plotted.

The variation of total-pressure ratio, adiabatic efficiency, and relative inlet Mach number at the mean radius of the rotor with equivalent tip speed is presented in figure 10 for design angle of attack and for peak efficiency at each speed.

The total-pressure ratio for design angle of attack increased steadily with tip speed up to 940 ft/sec where the pressure ratio was 1.37, $\eta = 0.92$, and $M_m = 0.90$. Above this tip speed, the total-pressure ratio decreased quite rapidly. The pressure ratios obtained for the peak efficiency conditions increased from 1.19 to 1.60 as Mach number increased from 0.63 to 1.06, and were everywhere higher than those obtained for design angle-of-attack conditions. The pressure-ratio curve flattened out at the higher Mach numbers corresponding to the reduction in efficiency with Mach number.

Peak efficiency remained constant at 0.96 up to a mean radius inlet Mach number of 0.87 and gradually decreased to 0.90 at a Mach number of 0.96 $\left(\frac{U_t}{\sqrt{\theta}} = 1060 \text{ ft/sec} \right)$ where total pressure ratio was 1.555. Design angle-of-attack efficiency coincided with peak efficiency at the lower tip speeds (M_m up to approximately 0.87). At the higher tip speeds and Mach numbers, efficiency at design angle of attack decreased more rapidly than did peak efficiency becoming 0.65 at $\frac{U_t}{\sqrt{\theta}} = 1060 \text{ ft/sec}$.

Hence, it may be concluded that efficient high-pressure-ratio transonic rotors can be designed for operation at mean radius inlet Mach numbers up to approximately 0.87 by using low-speed cascade data; for operation at higher inlet Mach numbers, low-speed cascade data must be supplemented with a more detailed examination of the transonic flow field.

Effect of Angle of Attack on Efficiency

In order to examine the effect of angle of attack on efficiency at constant Mach number, rotor efficiency is plotted against rotor inlet Mach number at the mean radius M_m for angles of attack α_m of 0° , 2° , and 4° above design in figure 11. The dashed curve represents the peak efficiencies plotted against M_m . For Mach numbers up to 0.87 peak efficiencies and those associated with angles of attack of 0° , 2° , and 4° above design were identical. Above $M_m = 0.87$ the design angle-of-attack efficiency decreased more rapidly with Mach number than did peak efficiency. For the entire Mach number range the efficiencies corresponding to $\alpha_m = 4^\circ$ above the design angle selected from low-speed cascade data were almost as high as the peak efficiencies.

Schlieren studies of flow.- In order to obtain information concerning the existence of shock waves ahead of the rotor at transonic speed, schlieren motion pictures were taken of the flow entering the rotor. Figure 12 presents a series of schlieren photographs showing the variation in shock position as the air equivalent tip speed was varied from 940 ft/sec to 1120 ft/sec with the throttle open. The region observed is bounded by a 1- by 1.1-inch mirror and the annulus height, and is 0.21 inch from the rotor leading edge. The vertical dark band on the left side of the pictures is the shadow of the knife edge and the dark spots in the upper right section are flaws in the optical system. In the movies a very weak and unstable shock flickered in and out of the picture in the upper left-

hand corner at $\frac{U_t}{\sqrt{\theta}} = 940$ ft/sec indicating the existence of a weak unstable shock when the mean radius inlet Mach number was 0.92. At approximately $\frac{U_t}{\sqrt{\theta}} = 980$ ft/sec the shock was definite and stable. (The Mach number was 0.96.) As tip speed increased, the shock became more distinct and moved closer to the leading edge of the blade.

The relative shock positions as obtained from the pictures in figure 12 corrected by the known small amount of light flash lag due to speed variation are shown to scale in figure 13. The blade sections shown are those at the mean radius. The Mach numbers M_m , $(\alpha - \alpha_d)_m$ values, and rotor efficiencies for the various tip speeds are indicated.

No shock is indicated for $\frac{U_t}{\sqrt{\theta}} = 940$ ft/sec since it was quite weak and unstable, as mentioned previously. As the inlet Mach number increased

~~CONFIDENTIAL~~

from $M_m = 0.92$ to 1.06 , the part of the shock visible in the mirror moved closer to the blade leading edge and at the same time turned approximately 20° . In order to determine whether these upstream shocks existed when the rotor efficiency was high, movies were made at a fixed tip speed of 1090 ft/sec while varying the throttle setting. Figure 14 presents the positions of the shocks obtained from the movies at several equivalent weight flows ranging from 21.4 to 24.2 lb/sec. As indicated in this figure, definite shocks were observed for all the weight flows and efficiencies ranging from 0.72 to 0.87 .

A comparison of shock location at two angles of attack for a constant M_m of 0.99 can be made by examining figures 13 and 14 at $\frac{U_t}{\sqrt{\theta}} = 1020$ ft/sec and throttle setting 4, respectively. The shock associated with the lower angle of attack $(\alpha - \alpha_d)_m = -0.4^\circ$, was approximately 20 percent closer to the blade leading edge than that associated with $(\alpha - \alpha_d)_m = 3^\circ$. The angle between the shock and the tangential direction remained constant at 48° for both angle-of-attack conditions. It is not obvious that the large increase in efficiency from 0.72 to 0.87 obtained with increasing angle of attack can be explained on the basis of the movement of the shock wave away from the blade leading edge at the higher angle-of-attack condition.

Comparison of flow conditions at $M_m = 0.99$ for $(\alpha - \alpha_d) = -0.4^\circ$ and $(\alpha - \alpha_d) = 3^\circ$. There is evidence from transonic isolated airfoil tests reported in references 10 and 11 that the angle of attack for maximum lift-drag ratio increased in the transition from subsonic to supersonic stream Mach number. These rotor tests have indicated a similar increase in angle of attack for peak efficiency. However, unlike the isolated airfoil phenomena the reasons for the observed rotor performance are believed to be mainly associated with cascade interference effects. In order to investigate the possibility of the concave surface becoming critical under the lower angle-of-attack conditions in the rotor, the required location of the inlet stagnation streamlines in order to accommodate the flow were estimated for $M_m = 0.99$ at $(\alpha - \alpha_d) = -0.4^\circ$ and 3° . This estimation was guided by the observed location of the shock waves and the geometric blade passage. It indicated that, in order to accommodate the higher weight flow associated with the lower angle of attack, the stagnation streamline would have to move outward resulting in a rather large negative local angle of attack in the leading-edge region. The amount of outward shift in stagnation streamline and hence the magnitude of this negative local angle of attack becomes larger as inlet Mach number increases toward 1.0 . In order to substantiate the

~~CONFIDENTIAL~~

existence of a large negative angle of attack in the leading-edge region, schlieren photographs of the NACA 65-(12A₂I₈₀)10 compressor blade section tested in the high-speed cascade tunnel at $\beta = 60^\circ$, $\sigma = 1$, and $(\alpha - \alpha_d) = 0.4^\circ$ at high subsonic Mach numbers were examined. Figure 15 presents one of these photographs for an inlet Mach number of 0.785. The flow direction at the stagnation point was obtained by bisecting the angle contained by the sharply defined compression region upstream of the leading edge. When this flow direction is compared with the far upstream flow direction it is clear that there is a large inward curvature of the stagnation streamlines. The inward curvature causes the blade to operate at a severe negative local angle of attack. The flow over the lower surface overexpands to supersonic velocities near the leading edge. This region is followed by shock waves. The thickness of the boundary layer behind the shock waves will increase with an increasing amount of diffusion along the blade surface. Hence, an evaluation of the change in this diffusion with angle-of-attack variation at constant Mach number is desirable. Unfortunately, there are no blade surface pressure distributions available at such high Mach numbers ($M_m = 0.99$) from which to obtain such information. However, the amount of diffusion that occurs along the blade surface should increase as the average amount of diffusion in the blade passage increases. Hence, at $M_m = 0.99$ the variation in amount of diffusion was computed for $(\alpha - \alpha_d) = -0.4^\circ$ and 3° on a one-dimensional isentropic basis. At the mean radius, the average Mach number at the minimum blade passage area A_T decreased from 0.76 to 0.62 as $(\alpha - \alpha_d)$ increased from -0.4° to $+3^\circ$. The ratio of downstream flow area A_2 to minimum passage area A_T is practically independent of α from $(\alpha - \alpha_d) = -0.4^\circ$ to $+3^\circ$ because of the negligible variation in discharge angle outside of the stall region. Hence, because of compressibility, as the average Mach number in the minimum passage area is increased, the amount of diffusion (expressed as the ratio of the static-pressure rise from A_T to A_2 over the dynamic pressure at A_T and herein called the diffusion coefficient) must increase. The isentropic values of this diffusion coefficient $\frac{P_2 - P_T}{q_T}$ calculated using the design exit flow direction for $(\alpha - \alpha_d) = -0.4^\circ$ and 3° were 0.646 and 0.567, respectively. Hence, for a constant inlet Mach number it has been shown that the average diffusion coefficient for the blade passage is increased by approximately 13 percent as angle of attack decreased from 3° above design to -0.4° below it. Corresponding to this increase in diffusion coefficient for the passage, the diffusion coefficient along the blade lower surface is also increased with decreasing angle of attack. Hence, in summation, poor lower surface performance is obtained when angle of attack is low

$(\alpha - \alpha_d) = -0.4^\circ$ at constant Mach number $M_m = 0.99$ because (1) the larger weight flow requires that the inlet stagnation streamlines be displaced outward so much that severe negative local angles of attack result and the flow expands very rapidly in the leading-edge region of the lower surface resulting in a local supersonic velocity region and shock waves, and (2) the larger diffusion coefficient for the lower surface associated with the lower angle of attack will tend to increase further the boundary-layer thickness behind the shocks and hence increase the likelihood of flow separation. As inlet Mach number decreases below 1.00 at constant α the lower surface performance should improve since both the magnitude of the local negative angle of attack will be less and the amount of diffusion along the blade surface will be less.

Estimation of the inlet stagnation streamline for the $(\alpha - \alpha_d) = 3^\circ$ condition at $M_m = 0.99$ indicated that for this flow the inlet stagnation streamlines were displaced so that positive local angles of attack resulted. Since the rotor efficiency did increase appreciably as α was increased, the overexpansion and the adverse pressure gradient in the leading-edge region of the upper surface associated with $(\alpha - \alpha_d) = 3^\circ$ were probably less than those occurring on the lower surface at $(\alpha - \alpha_d) = -0.4^\circ$. Examination of pressure distributions from high-speed cascade tests of a 65-(12A₂I_{8b}) 10 at $\beta = 60^\circ$ and $\sigma = 1$ corroborated these conclusions.

Resume of remarks regarding effects of angle of attack on efficiency.-

It is indicated in figure 11 that below $M_m = 0.87$ the deviation between design angle-of-attack efficiency and peak efficiency was negligible. Above $M_m = 0.87$ the deviation increased monotonically with Mach number.

This rapid reduction in design angle-of-attack efficiency with Mach number can be explained on the basis of the previous discussion which indicated that, at the design angle of attack selected from low-speed cascade data, the severity of the operating conditions for the blade lower surface increased as inlet Mach number increased. It has been shown that the lower surface operating conditions could be made less severe at transonic inlet Mach numbers by increasing the angle of attack several degrees. The amount of improvement in lower surface performance obtained by increasing the angle of attack 4° above design more than compensates for any associated decline in upper surface performance. The increase in efficiency with angle of attack at constant inlet Mach number will continue until α is so high that severe velocity peaks occur over the leading-edge region and flow separation results.

Determination of the Effect of Mean Radius Rotor Inlet

Mach Number and Reynolds Number on Turning Angle

Mean radius corrected turning angle plotted against mean radius inlet Mach number is presented in figure 16. The circles indicate air tests and the squares, Freon tests. The turning angle obtained from low-speed cascade tests is indicated. From $M_m = 0.10$ to 0.85 there was essentially no change in turning angle from that predicted by low-speed cascade tests. From $M_m = 0.85$ to 1.10 the turning angle decreased approximately 1.3° . There was no significant effect on turning angle in changing from air to Freon as a testing medium.

Corrected turning angles at the mean radius plotted against Reynolds number are presented in figure 17. Over the entire range of Reynolds numbers from 1.2×10^5 to 9.2×10^5 the corrected turning angle remained constant. Hence, there appeared to be no laminar separation of the flow even at the low Reynolds numbers. Again there was no significant effect on corrected turning angle in changing from air to Freon as a testing medium.

Comparison Between Mean Radius Measured Turning Angles

of Rotor Tests and Low-Speed Cascade Tests

The turning angles at the mean radius, obtained from the Freon tests, are plotted against corrected mean radius angles of attack and are presented in figure 18(a). Since these turning angles were obtained for mean radius inlet Mach numbers ranging from 0.86 to 1.04 and there is some variation in turning angle with Mach number, the resulting scatter necessitated that the measured turning angles be presented as a shaded region in this figure. The low-speed cascade data for the A-series blades (ref. 4) were used to estimate the relation between ϕ and α_c .

Figure 18(b) presents the rotor data corrected to constant axial velocity by the method previously described in this report. The two-dimensional low-speed cascade data agreed very well with the corrected turning-angle data in the angle-of-attack region ranging from 12° to 14° . At 10.6° , the design angle of attack selected from low-speed cascade data, the cascade predicted turning angle was about 2° too high.

One possible explanation for the lower turning angles at low angles of attack was obtained from an examination of some unpublished high-speed cascade data obtained for an NACA 65-(12A₂I_{8b})10 blade section at an inlet-air angle of 45° and a solidity of 1.5 . These data indicated that the turning angle decreased more rapidly with increasing Mach number at

~~CONFIDENTIAL~~

low angles of attack than at design angle of attack. This decrease in turning angle with Mach number at the low angles of attack could explain why the high-speed rotor turning angles were several degrees below those of the low-speed cascade in the low angle-of-attack region. Another factor, which probably contributes to lower turning angles for the rotor tests at lower angles of attack, is the fact that at low angles of attack there is a greater centrifuging of the thick hub boundary layer (thick because of the secondary flow of case boundary layer). This centrifuged boundary layer could encompass the mean radius section at low angles of attack and thereby reduce mean radius turning angles below those obtained in cascade tests.

Comparison of High Mach Number Performance of NACA $A_{2I_{8b}}$ -Series
and NACA A_{10} -Series Compressor Blade Sections

The rotor described in this report and the rotor discussed in reference 1 were designed to produce approximately the same pressure ratio. The mean radius σC_L for the rotor described in this report was 5 percent less than that for the rotor of reference 1. The major difference was that this rotor used NACA $A_{2I_{8b}}$ -series blades and that of reference 1 used NACA A_{10} -series blade sections. There were other design differences such as the NACA $A_{2I_{8b}}$ -series rotor solidity was constant at a value of 1.0, hub-tip ratio was 0.75, and tip diameter was 16 inches while the NACA A_{10} -series rotor had a constant solidity of 1.2, an inlet hub-tip ratio of 0.80, and a tip diameter of 14 inches. The maximum camber for the NACA A_{10} -series rotor was 1.4 while that of the NACA $A_{2I_{8b}}$ -series rotor was 1.85.

Figure 19 represents a comparison of the performance of these two rotors. The NACA A_{10} -series rotor data are plotted as the dashed curves. Rotor peak efficiency and the corresponding total pressure ratios are plotted against relative inlet Mach number entering the rotor at the mean radius. The NACA $A_{2I_{8b}}$ -series rotor maintained approximately constant efficiency (0.96) from $M_m = 0.63$ to $M_m = 0.87$. The NACA A_{10} -series rotor had a gradual drop in efficiency of approximately 7 percent for the same Mach number range. The total-pressure ratio obtained at 90 percent efficiency was 1.375 for the NACA A_{10} -series rotor as compared with 1.555 for the NACA $A_{2I_{8b}}$ -series rotor.

Hence, the NACA $A_{2I_{8b}}$ -series blades maintain high efficiency to a higher Mach number and pressure ratio level than the NACA A_{10} -series

blades. Because the NACA $A_{2I_{8b}}$ -series rotor had a lower hub-tip ratio, when the mean radius Mach numbers are the same as those for the NACA A_{10} -series rotor, the tip Mach number was higher and the hub Mach number was lower. Though the above-mentioned differences do exist between the two rotors, the comparative results are considered to be indicative of the relative performance characteristics of NACA $A_{2I_{8b}}$ - and A_{10} -series blade sections.

It should be noted that, for the same inlet air angle and solidity conditions, the minimum passage area between NACA $A_{2I_{8b}}$ -series blades is less than that for NACA A_{10} -series blades. Hence, the NACA $A_{2I_{8b}}$ -series blades are more susceptible to choking at low inlet air angles, high solidities, and high subsonic Mach numbers. For such applications the passage between blades should be checked for possible choking. The possibility of choking is reduced as the angle of attack increases. For the NACA $A_{2I_{8b}}$ blades these tests have indicated that peak efficiency occurred 4.0° above the design angle of attack obtained from low-speed cascade tests. Hence, if the values of design angles of attack are increased accordingly, the choking problem will be reduced in importance over that encountered when the design angles of attack are selected solely from low-speed cascade tests. This problem of choking is discussed in reference 4 wherein comparisons between NACA A_{10} , $A_{2I_{8b}}$ series, and other mean-line airfoils are made. One method of reducing the choking problem at low inlet angles and high solidities would be to use a thickness distribution other than the NACA 65 series with the NACA $A_{2I_{8b}}$ mean lines. Of course, care must be taken that such changes in thickness distribution and meanline shape do not introduce other effects detrimental to good performance. Another solution for low inlet angles and high solidities is to use a meanline intermediate between the NACA A_{10} and the $A_{2I_{8b}}$ series with no change in thickness distribution. In some applications, it may be necessary to use both methods suggested above.

SUMMARY OF RESULTS

The following results were obtained from an experimental investigation of an axial-flow compressor rotor which had NACA $A_{2I_{8b}}$ -series blade sections and was designed to operate efficiently at high speeds:

1. Efficient high-pressure-ratio transonic rotors can be designed using low-speed cascade data for operation at mean radius inlet Mach

~~CONFIDENTIAL~~

numbers up to approximately 0.87 since peak efficiency and design angle-of-attack efficiency were coincident up to this Mach number.

2. Above the mean radius inlet Mach number of 0.87 peak efficiency gradually decreased from 0.96 to 0.90 at a Mach number of 0.96 and a total pressure ratio of 1.555 whereas design angle-of-attack efficiency decreased more rapidly with Mach number.

3. The efficiencies corresponding to angles of attack 4.0° above design and peak efficiencies were quite similar over the entire Mach number range tested.

4. Two-dimensional low-speed cascade data agreed very well with the high-speed rotor corrected turning-angle data in the angle-of-attack region ranging from 12° to 14° . At 10.6° , the design angle of attack obtained from low-speed cascade data, the cascade predicted turning angle was about 2° too high.

5. The shift in peak efficiency to higher-than-design angles of attack for mean radius inlet Mach numbers above 0.87 may have resulted because (1) the severity of the operating conditions for the blade lower surface increased as inlet Mach number approached the transonic range, and (2) the amount of improvement in lower surface performance obtained by increasing the angle of attack 4.0° above design in the transonic Mach number range more than compensated for any associated decline in upper surface performance.

6. At a mean radius inlet-air angle of 60° , the effect of inlet Mach number on turning angle was negligible from Mach numbers of 0.10 to 0.85. From 0.85 to 1.10 the turning angle decreased approximately 1.3° .

7. The mean radius turning angles measured were independent of Reynolds numbers in the range tested from 1.2×10^5 to 9.2×10^5 at $M_m = 0.61$.

8. The mean radius turning angles were independent of whether the testing medium was air or Freon in the range tested.

9. A comparison between two rotors designed for the same pressure ratio with one using NACA A_{218b} -series blades and the other using NACA

A₁₀-series blades indicated that the NACA A₂I_{8b}-series blades maintained high efficiency to a higher inlet Mach number level than did the NACA A₁₀-series blades.

Langley Aeronautical Laboratory,
National Advisory Committee for Aeronautics,
Langley Field, Va., June 19, 1953.

REFERENCES

1. Dugan, Paul D., Mahoney, John J., and Benser, William A.: Effect of Mach Number on Performance of an Axial-Flow Compressor Rotor-Blade Row. NACA RM E8D29, 1948.
2. Voit, Charles H., Guentert, Donald C., and Dugan, James F.: Performance of High-Pressure-Ratio Axial-Flow Compressor Using Highly Cambered NACA 65-Series Blower Blades at High Mach Numbers. NACA RM E50A09, 1950.
3. Voit, Charles H., Guentert, Donald C., and Dugan, James F.: Effect of Mach Number on Over-All Performance of Single-Stage Axial-Flow Compressor Designed for High Pressure Ratio. NACA RM E50D26, 1950.
4. Erwin, John R., Savage, Melvyn, and Emery James C.: Two-Dimensional Low-Speed Cascade Investigation of NACA Compressor Blade Sections Having a Systematic Variation in Mean-Line Loading. NACA RM L53I30b, 1953.
5. Erwin, John R., and Yacobi, Laura A: Method of Estimating The Incompressible-Flow Pressure Distribution of Compressor Blade Sections at Design Angle of Attack. NACA RM L53F17, 1953.
6. Westphal, Willard R., and Godwin, William R.: Comparison of NACA 65-Series Compressor-Blade Pressure Distributions and Performance in a Rotor and a Cascade. NACA RM L51H20, 1951.
7. Boxer, Emanuel, and Erwin, John R.: Investigation of a Shrouded and Unshrouded Axial-Flow Supersonic Compressor. NACA RM L50G05, 1950.
8. Huber, Paul W., and Kantrowitz, Arthur: A Device for Measuring Sonic Velocity and Compressor Mach Number. NACA TN 1664, 1948.
9. Lieblein, Seymour, Lewis, George W., Jr., and Sandercock, Donald M.: Experimental Investigation of An Axial-Flow Compressor Inlet Stage Operating at Transonic Relative Inlet Mach Numbers. I - Over-All Performance of Stage With Transonic Rotor and Subsonic Stators up to Rotor Relative Inlet Mach Number of 1.1. NACA RM E52A24, 1952.
10. Daley, Bernard N., and Dick, Richard S.: Effect of Thickness, Camber, and Thickness Distribution on Airfoil Characteristics at Mach Numbers up to 1.0. NACA RM L52G31a, 1952.
11. Nelson, Warren H., and McDevitt, John B.: The Transonic Characteristics of 17 Rectangular, Symmetrical Wing Models of Varying Aspect Ratio and Thickness. NACA RM A51A12, 1951.

TABLE I
BLADE SECTION COORDINATES FOR NACA A_2I_{60} -SERIES TRANSONIC ROTOR

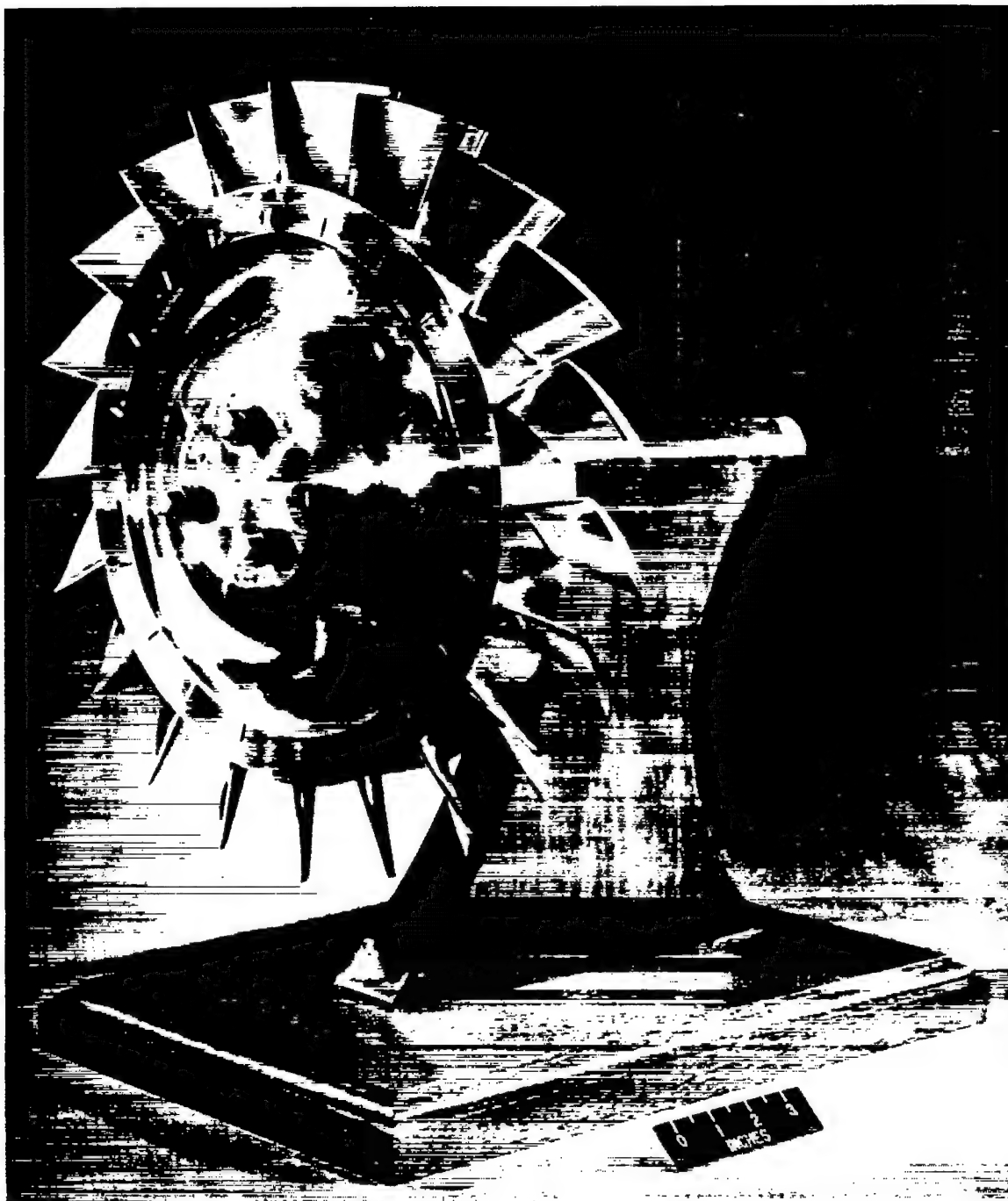
Hub section		
X	Y_U	Y_L
0.000	0.000	0.000
.009	.021	-.009
.014	.026	-.011
.024	.033	-.014
.047	.047	-.016
.094	.070	-.015
.141	.091	-.012
.189	.110	-.009
.283	.145	.002
.377	.177	.017
.471	.206	.033
.566	.231	.049
.660	.254	.065
.754	.273	.081
.848	.287	.097
.943	.297	.113
1.037	.304	.128
1.131	.304	.141
1.225	.300	.152
1.320	.289	.157
1.414	.274	.157
1.508	.250	.149
1.602	.217	.130
1.700	.172	.099
1.791	.115	.055
1.885	0	0
Leading-edge radius 0.012 Trailing-edge radius 0.019		

Mean radius section		
X	Y_U	Y_L
0.000	0.000	0.000
.011	.019	-.011
.017	.024	-.015
.028	.031	-.018
.055	.044	-.023
.110	.063	-.024
.165	.081	-.025
.220	.097	-.024
.330	.126	-.021
.440	.152	-.013
.550	.174	-.005
.660	.194	.005
.770	.211	.015
.880	.226	.026
.990	.236	.038
1.100	.243	.050
1.210	.245	.062
1.319	.245	.073
1.429	.238	.083
1.539	.228	.090
1.649	.214	.092
1.759	.195	.089
1.869	.168	.078
1.979	.134	.059
2.089	.091	.030
2.199	0	0
Leading-edge radius 0.014 Trailing-edge radius 0.022		

Tip section		
X	Y_U	Y_L
0.000	0.000	0.000
.013	.018	-.013
.019	.023	-.016
.031	.028	-.019
.063	.040	-.026
.126	.059	-.030
.189	.074	-.033
.251	.088	-.035
.377	.113	-.035
.503	.134	-.032
.628	.153	-.028
.754	.169	-.023
.880	.183	-.016
1.005	.194	-.008
1.131	.202	.001
1.257	.206	.010
1.382	.207	.020
1.508	.204	.030
1.634	.198	.039
1.759	.189	.047
1.885	.176	.050
2.010	.160	.048
2.136	.139	.043
2.262	.111	.032
2.387	.076	.012
2.513	0	0
Leading-edge radius 0.010 Trailing-edge radius 0.025		

CONFIDENTIAL

NACA RM L53G02



L-64407

Figure 1.- NACA A₂I_{8b}-series transonic rotor.

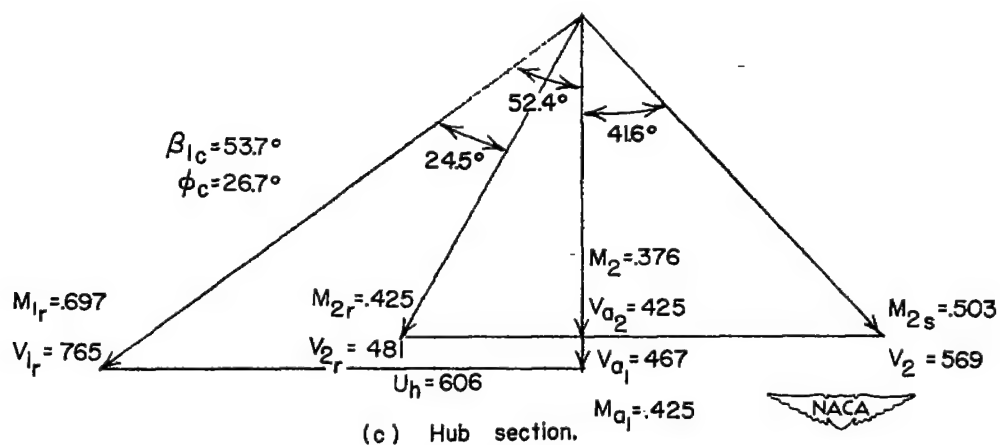
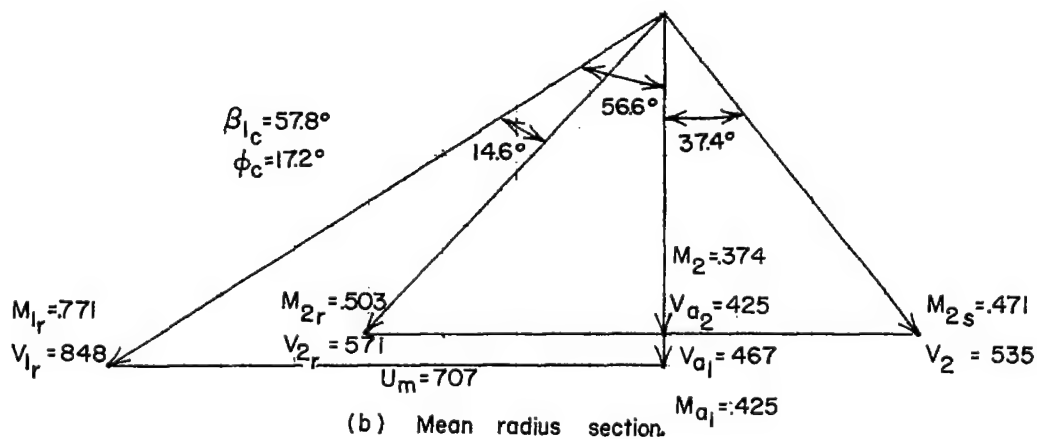
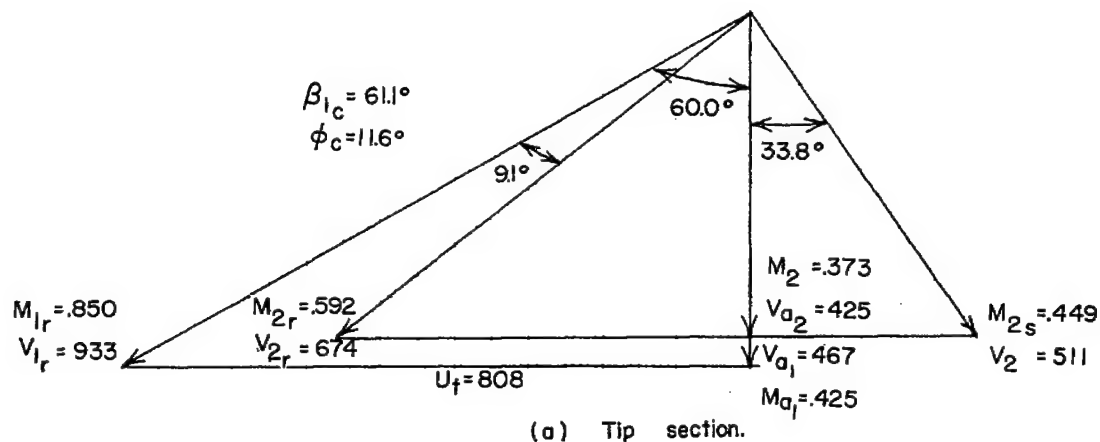


Figure 2.- Design velocity diagrams for compressor rotor.

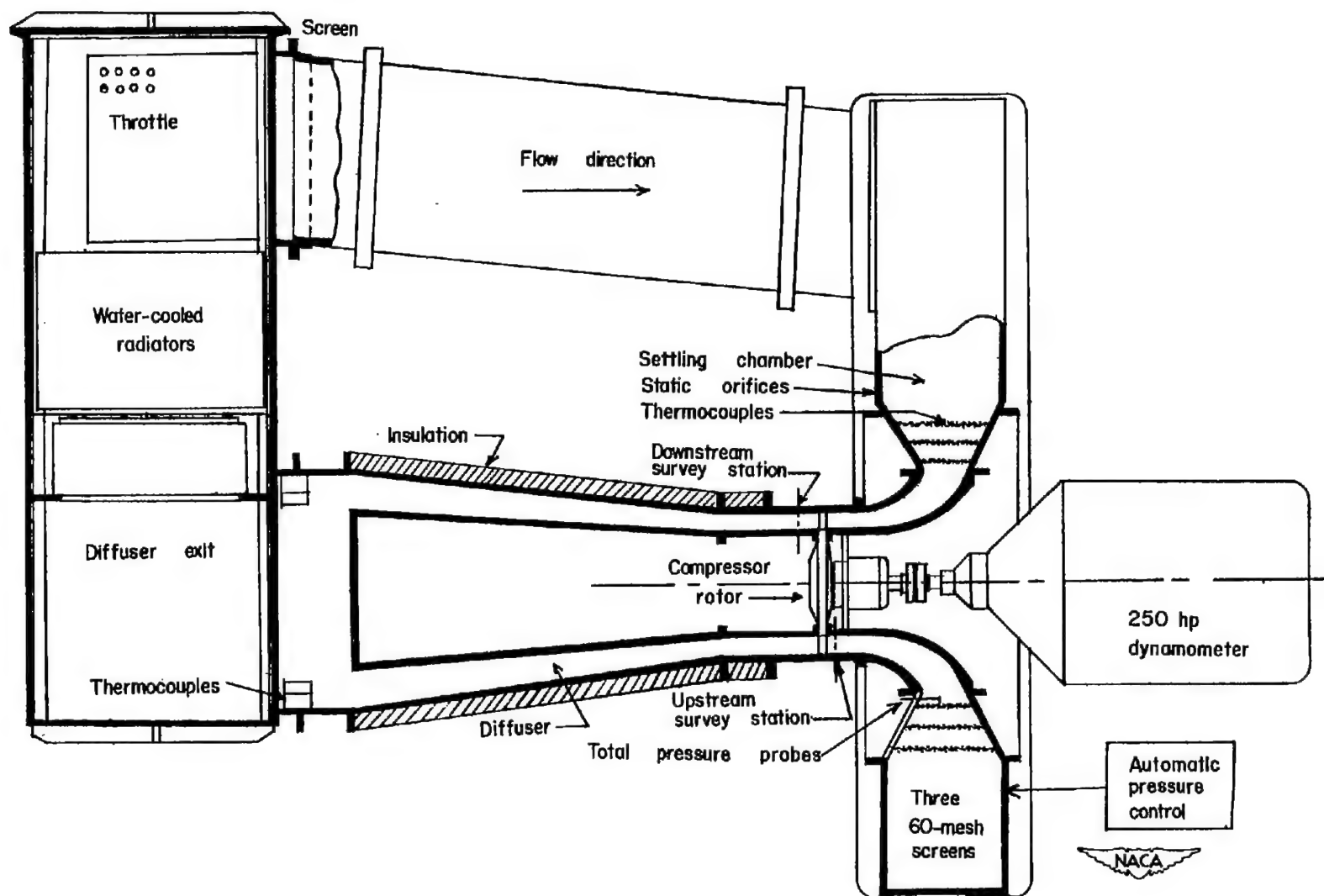


Figure 3.- Plan view of the 250-horsepower compressor test stand.

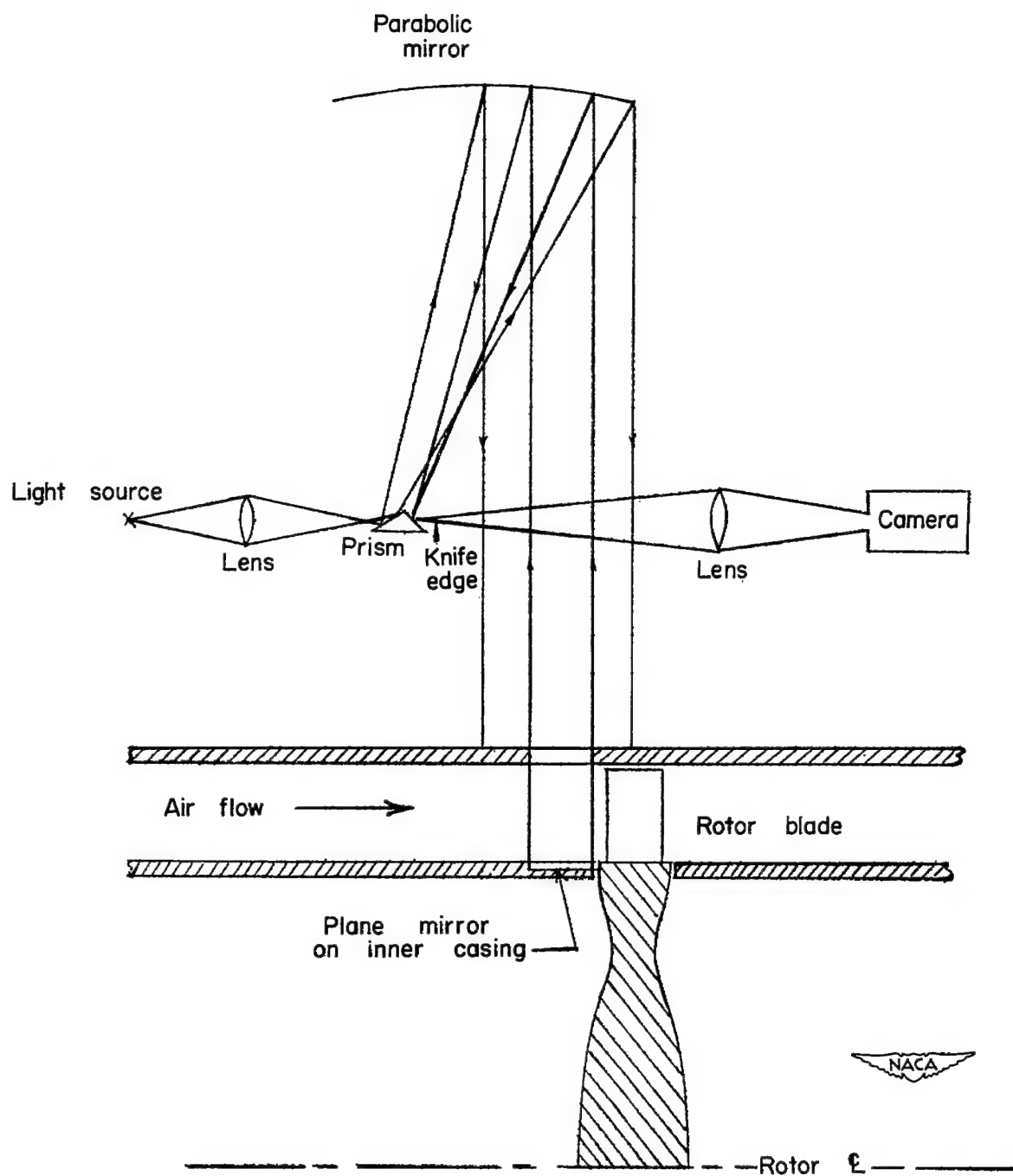


Figure 4.- Schematic of schlieren system used to obtain shock pattern upstream of rotor.

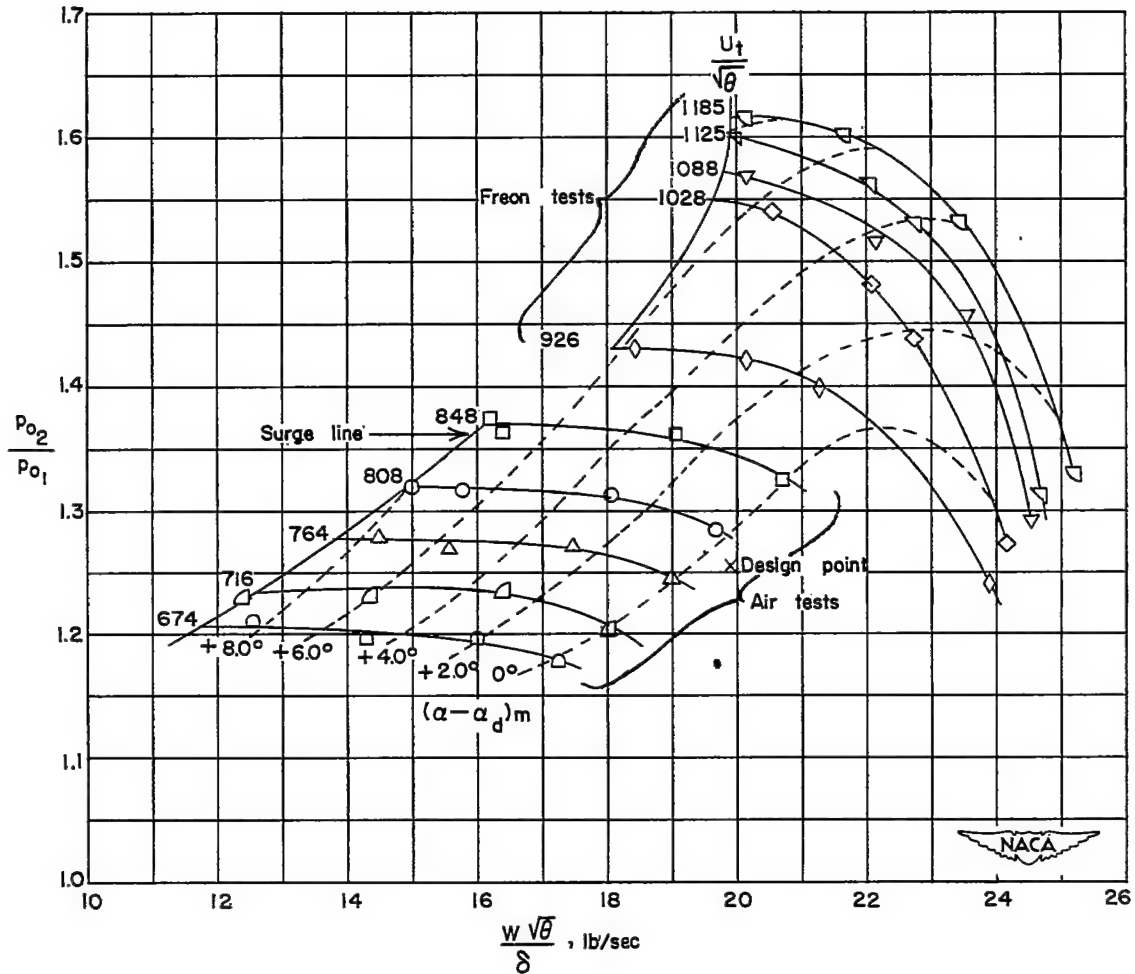


Figure 5.- Rotor performance characteristics in which total-pressure ratio, weight flow, and tip speed are all converted to air equivalent values and are corrected to standard inlet conditions.

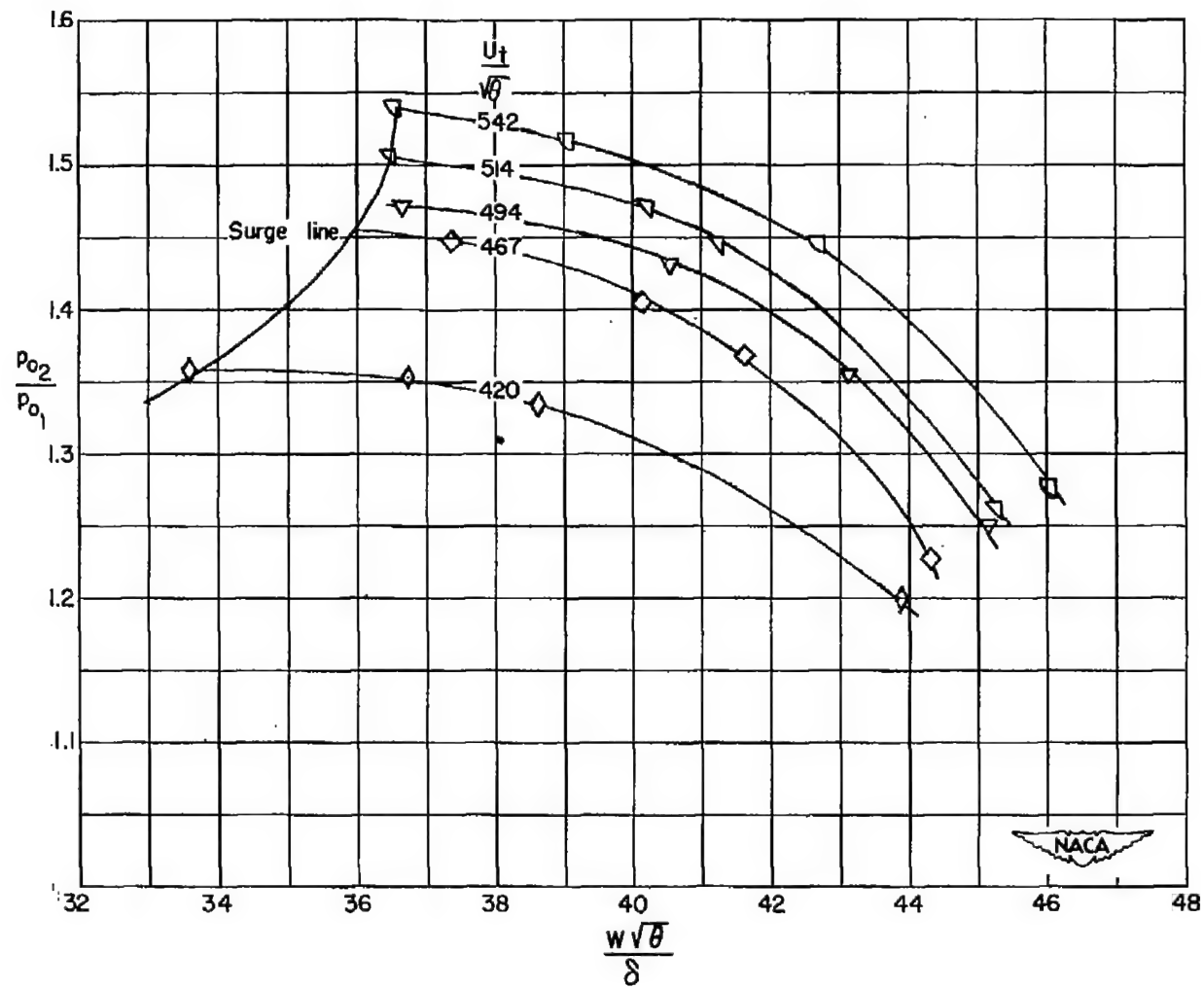


Figure 6.- Rotor performance characteristics in which total-pressure ratio, weight flow, and tip speed are Freon test values corrected to standard inlet conditions.

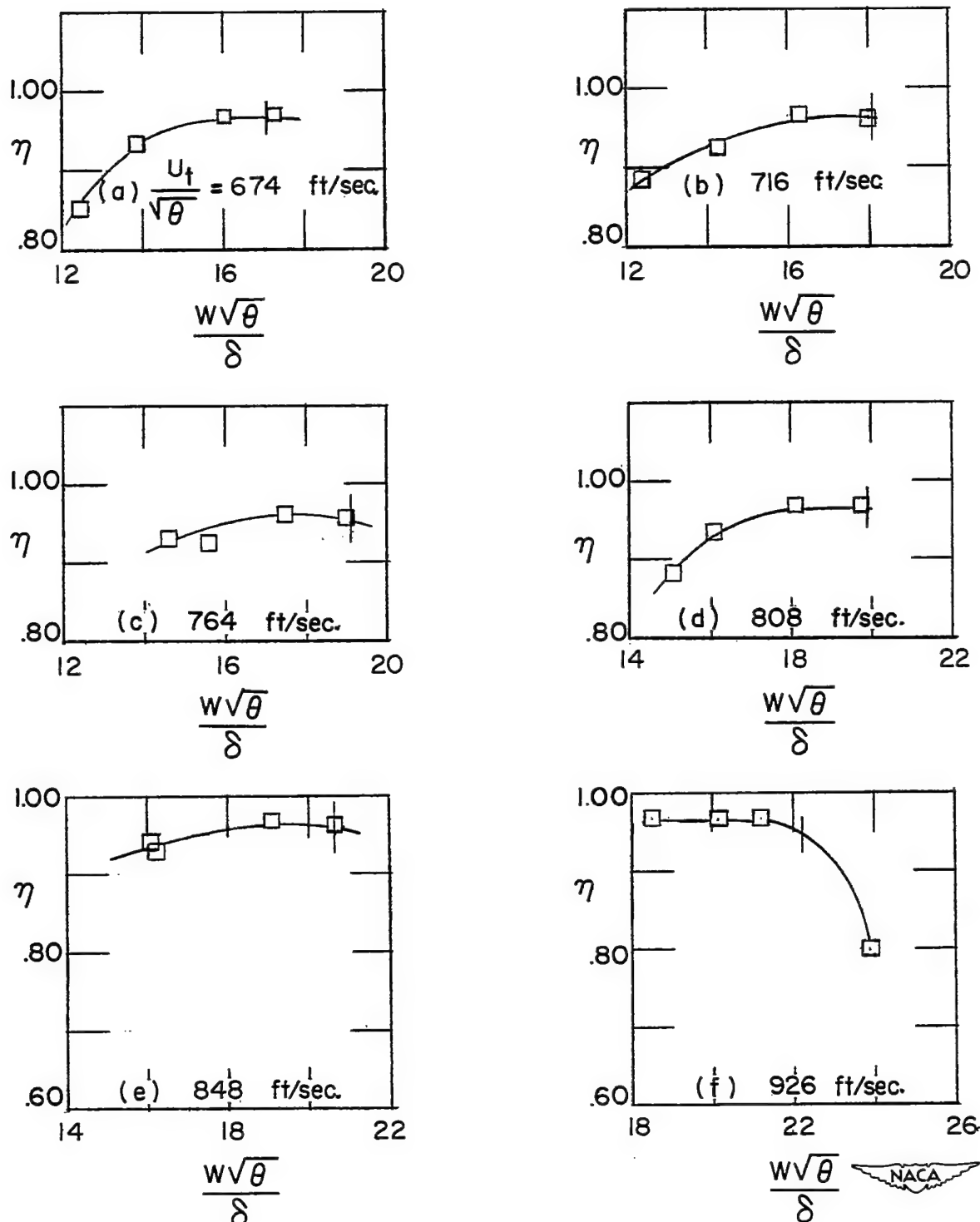


Figure 7.- Adiabatic rotor efficiencies plotted against air equivalent weight flow for the various test air equivalent tip speeds. Short vertical bars indicate design angle of attack at mean radius.

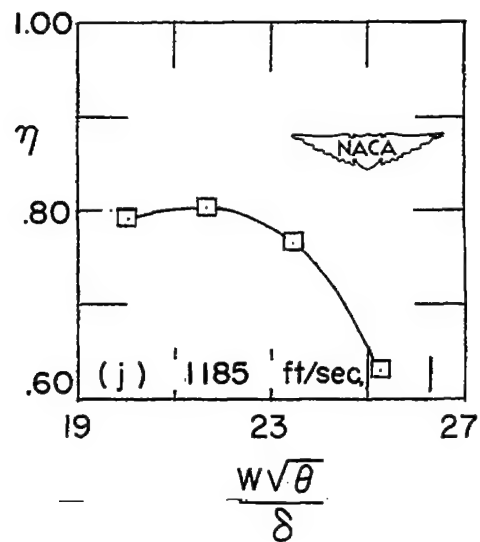
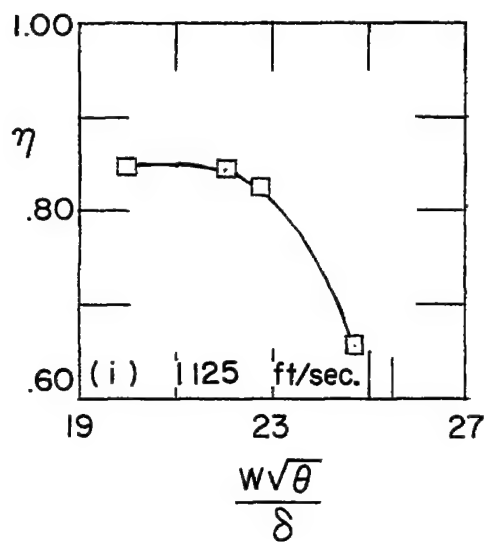
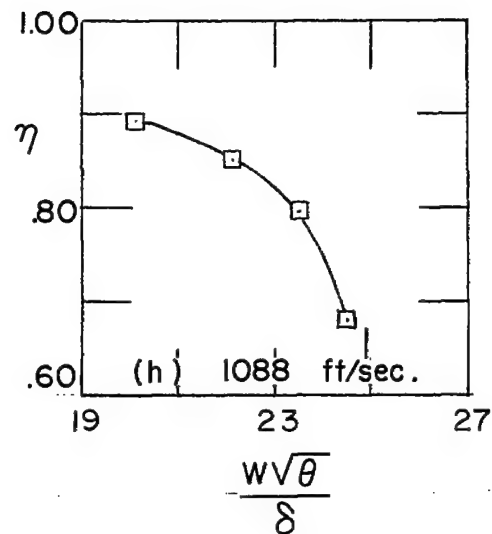
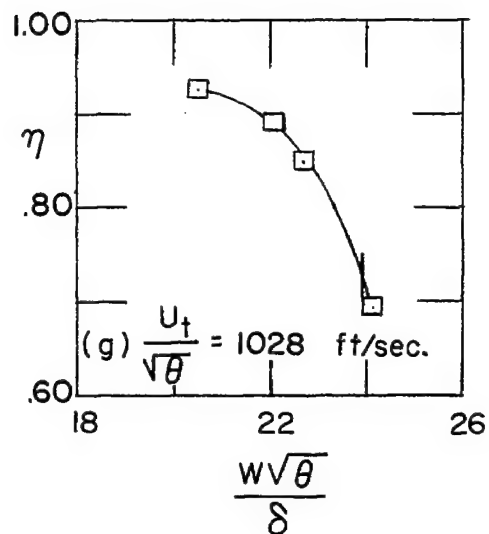


Figure 7.- Concluded.

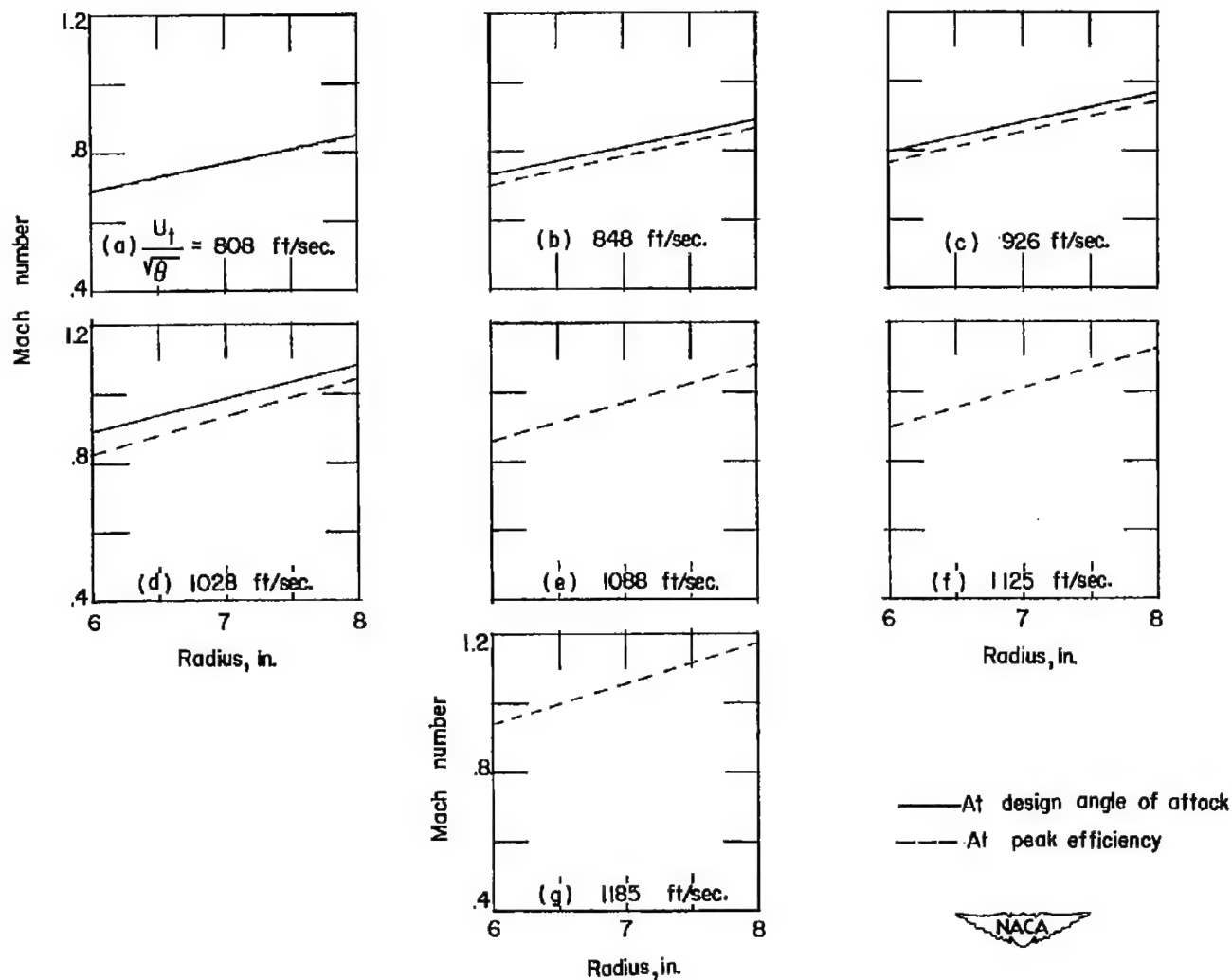


Figure 8.- Variation in rotor inlet relative Mach numbers with radius at corrected weight flows corresponding to peak efficiency and mean radius design angle of attack for the tip speeds at and above design speed.

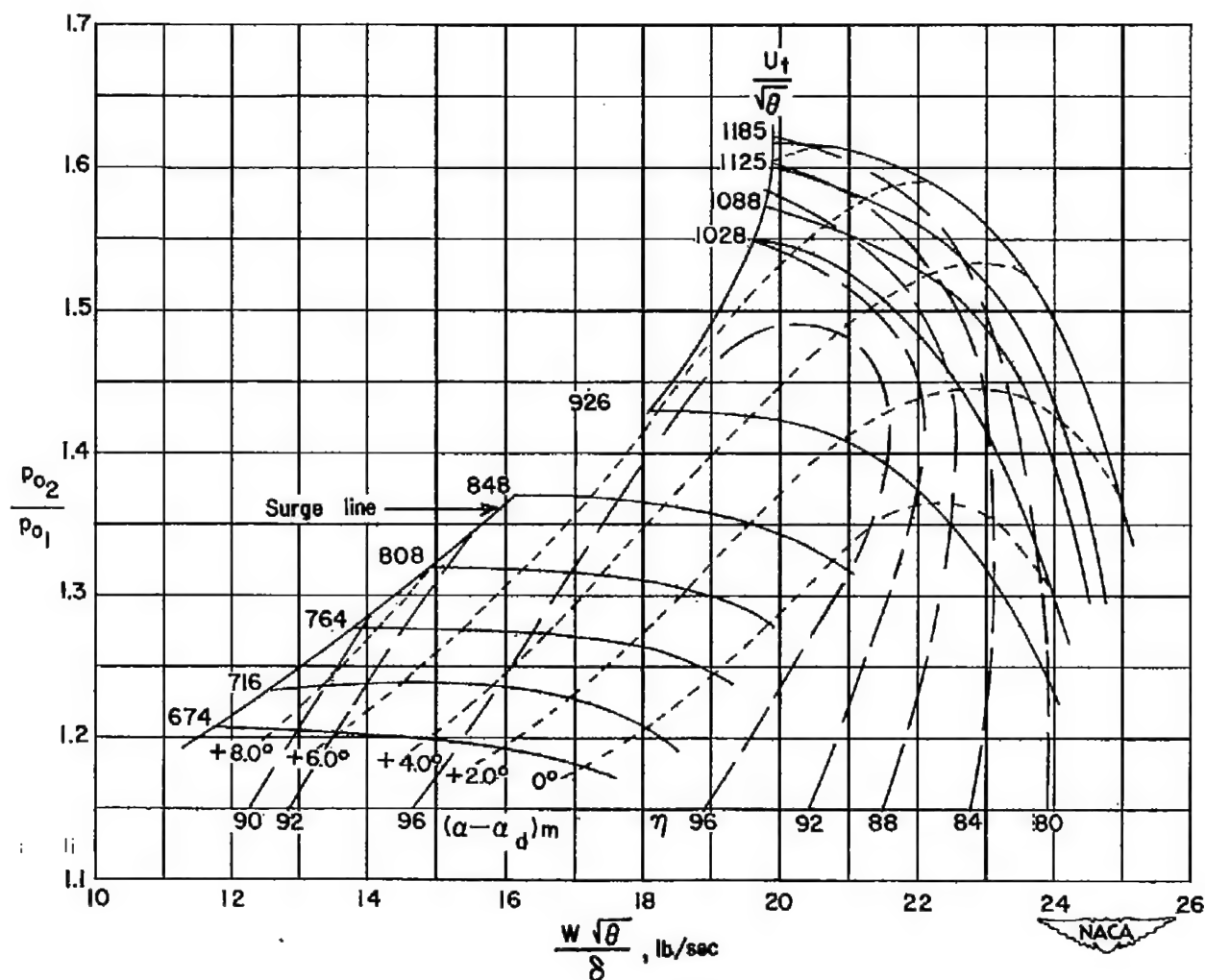


Figure 9.- Rotor performance characteristics and efficiency contours in which total-pressure ratio, weight flow, and tip speed are all converted to air equivalent values and are corrected to standard inlet conditions.

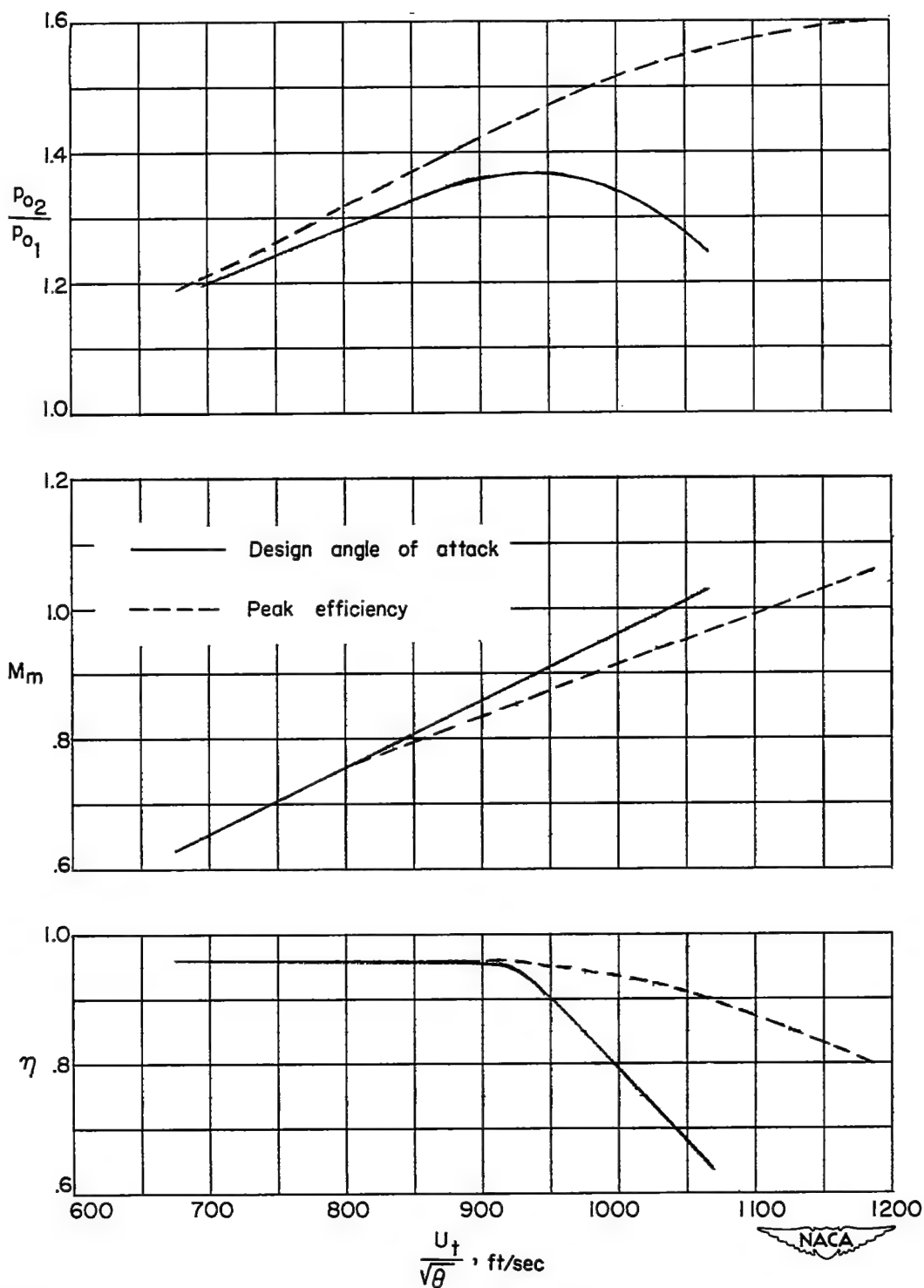


Figure 10.- Variation in total-pressure ratio, relative inlet Mach number at the mean radius, and rotor efficiency with tip speed.

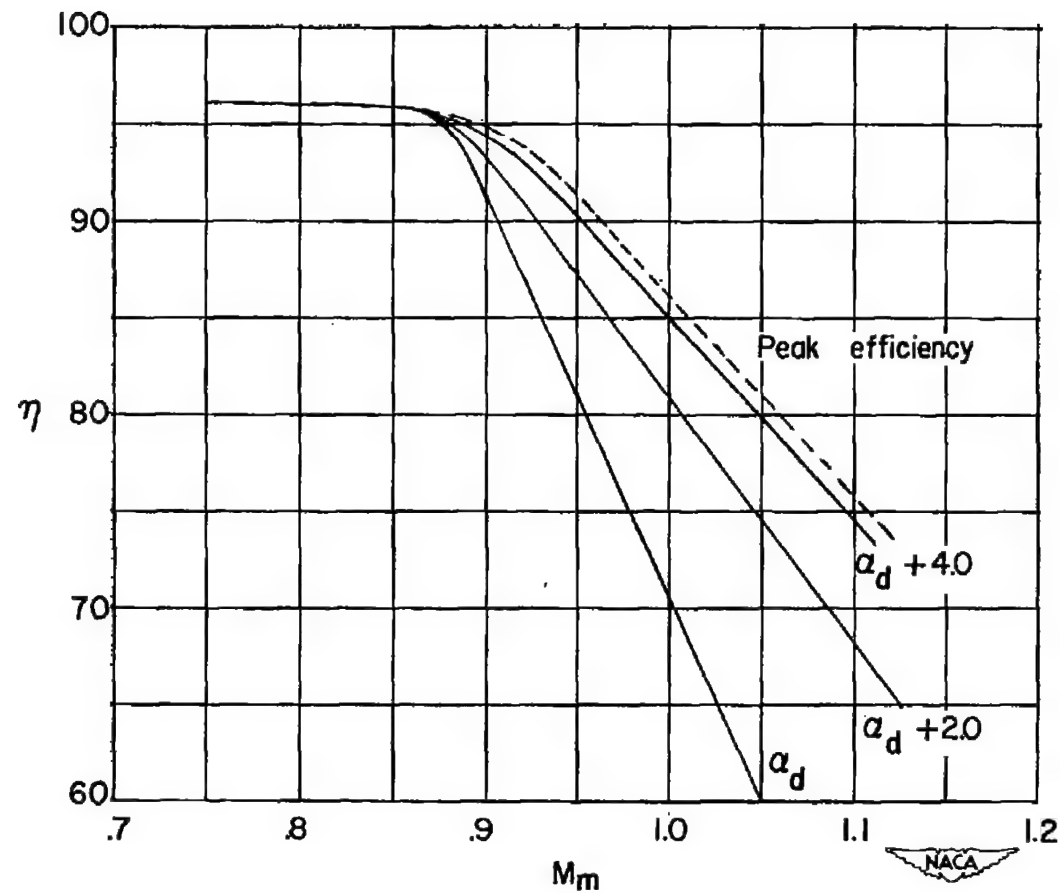
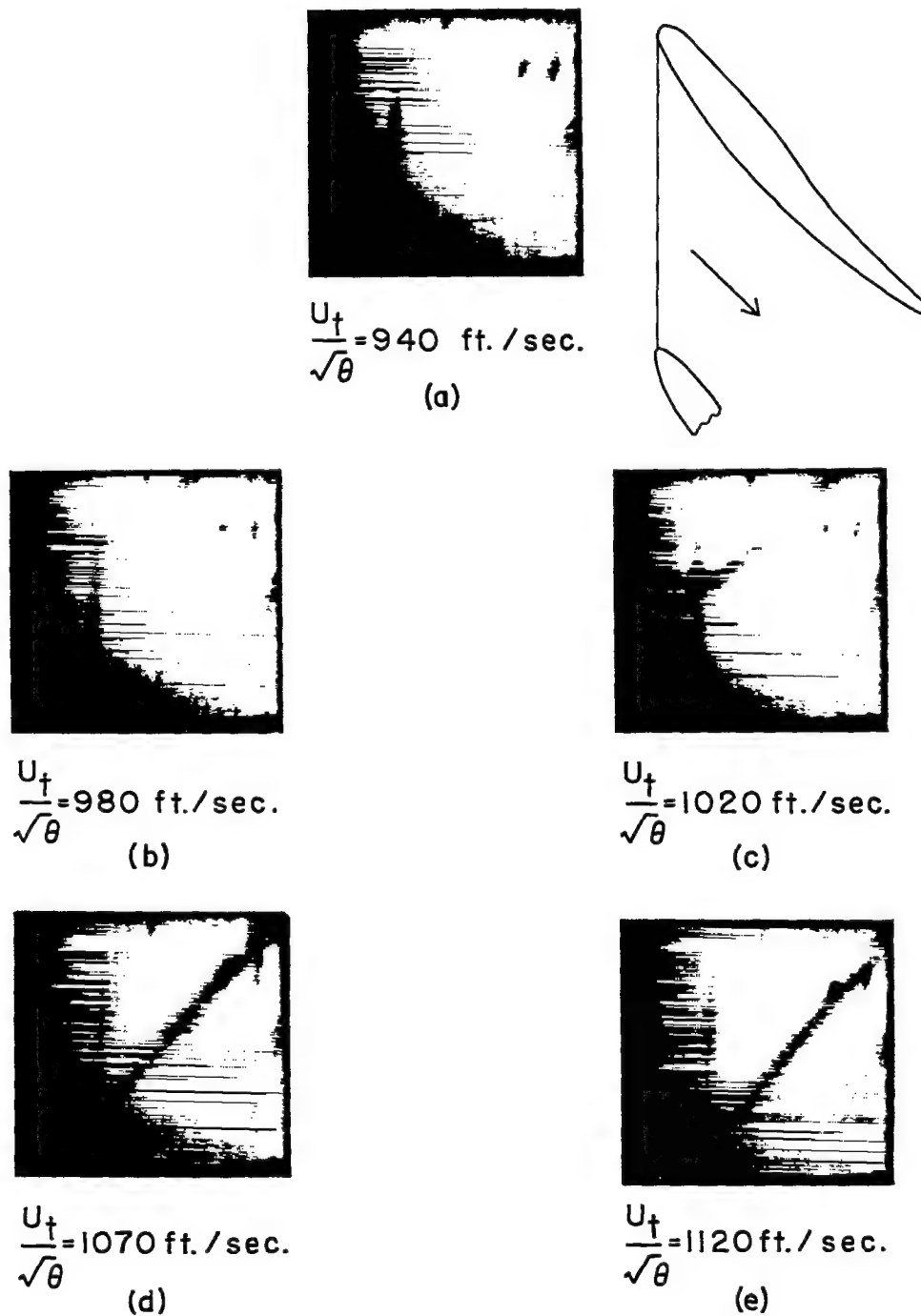


Figure 11.- Variation in rotor efficiency with Mach number at the mean radius for various mean radius angles of attack.



L-80210

Figure 12.- Photographs obtained from motion pictures of the variation in shock location with tip speed at open throttle.

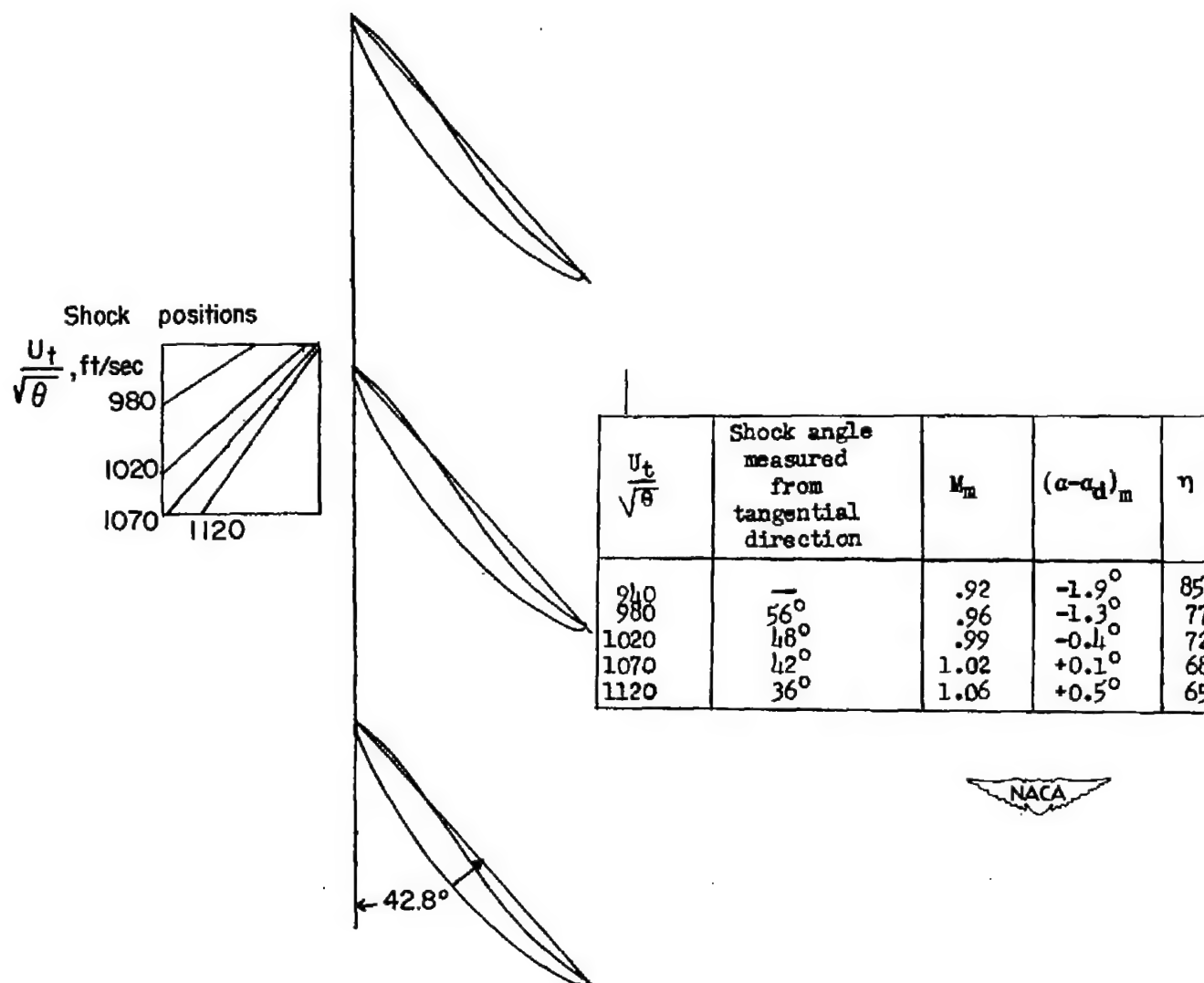


Figure 13.- Variation in shock position with corrected rotational speed at open throttle setting.

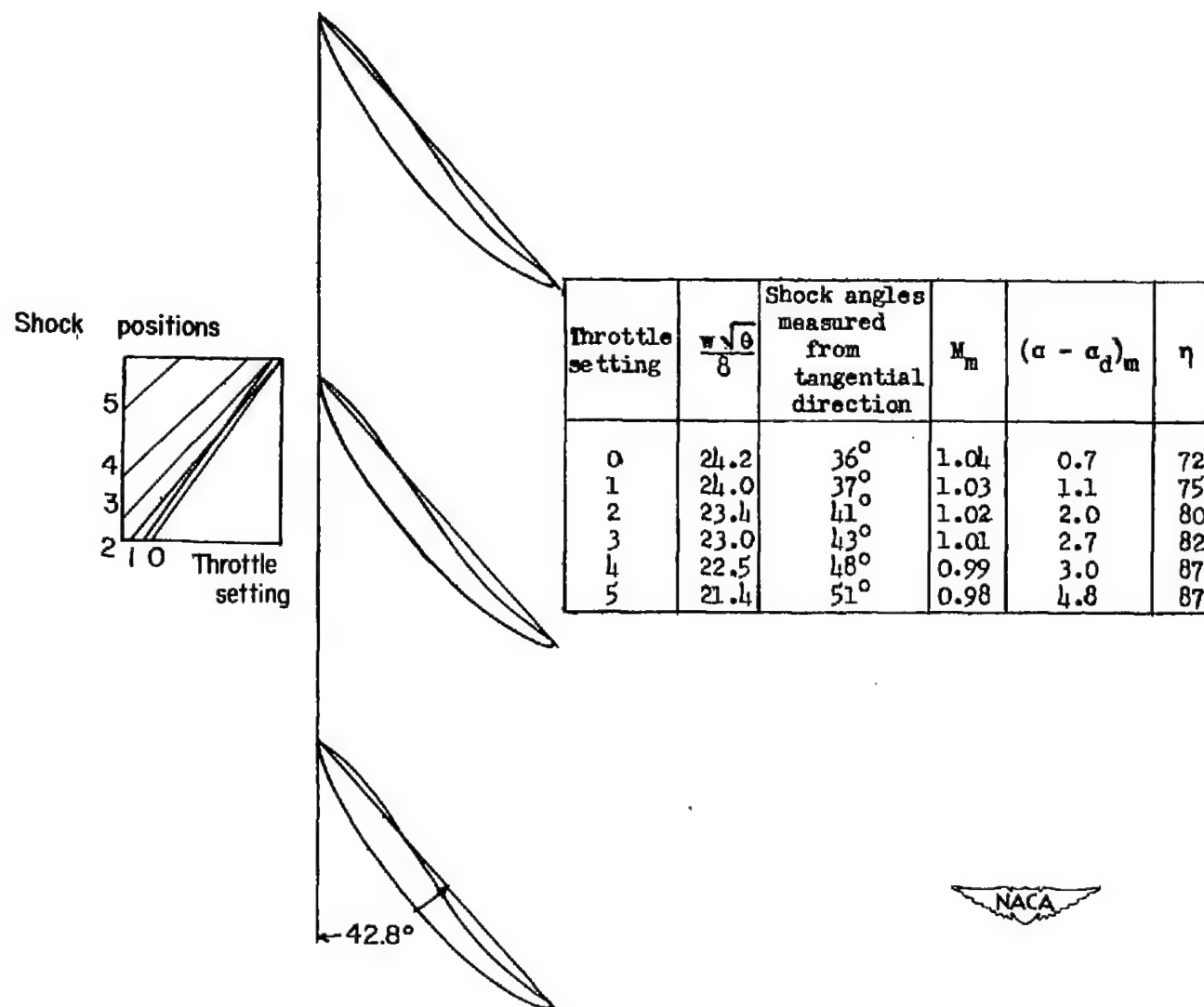


Figure 14.- Variation in shock position with throttle setting at a corrected tip speed of 1090 feet per second.



L-80209

Figure 15.- Schlieren photograph of NACA 65-(12A₂I8_b)10 blade section at $\beta = 60$, $\sigma = 1.0$, $M = 0.785$, and $(\alpha - \alpha_d) = 0.4^\circ$.

~~CONFIDENTIAL~~

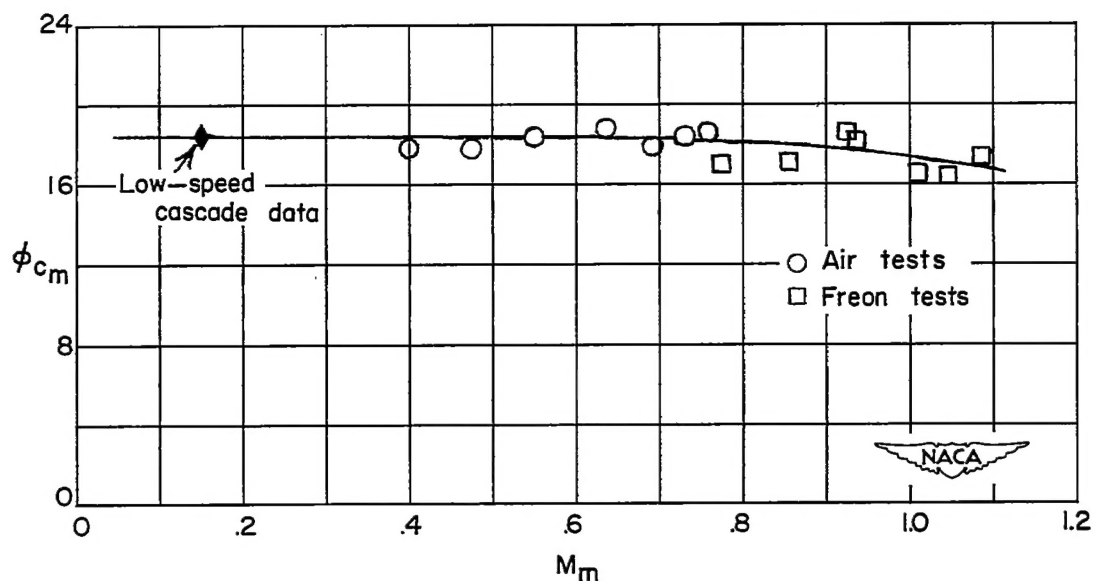


Figure 16.- Variation in corrected turning angle with inlet Mach number at the mean radius for $\beta_c = 60^\circ$ and $\alpha_c = 12.8^\circ$.

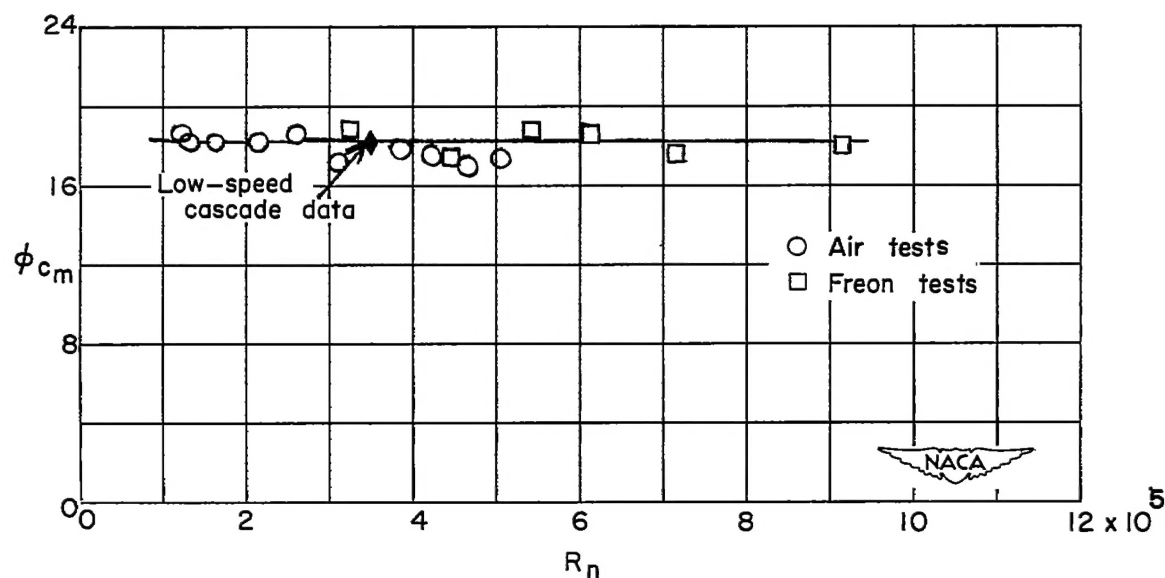
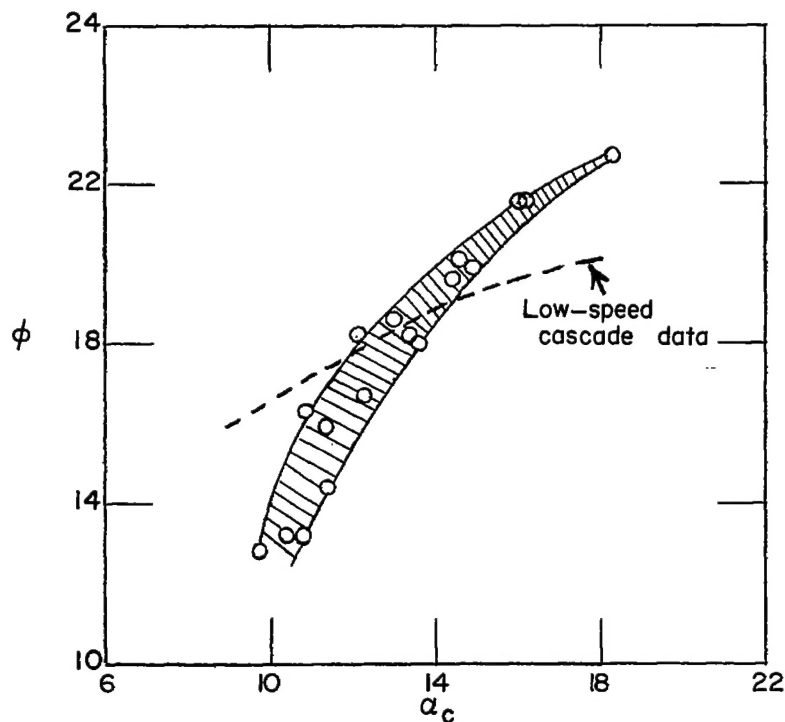
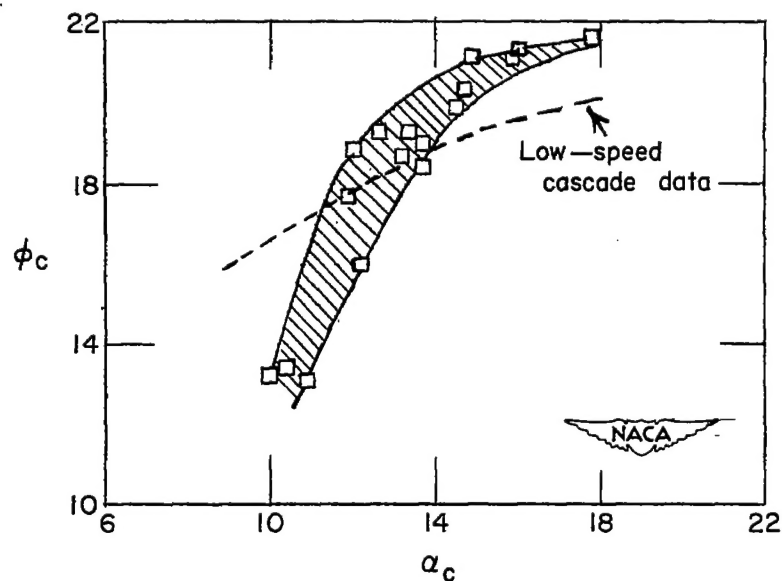


Figure 17.- Variation in corrected turning angle with Reynolds number at the mean radius for $\beta_c = 60^\circ$, $\alpha_c = 12.8^\circ$, and $M_m = 0.61$.



(a) Turning angle not corrected.



(b) Corrected turning angle.

Figure 18.- Comparison, at the mean radius, of variation in turning angle with corrected angle of attack for Freon tests and low-speed cascade tests.

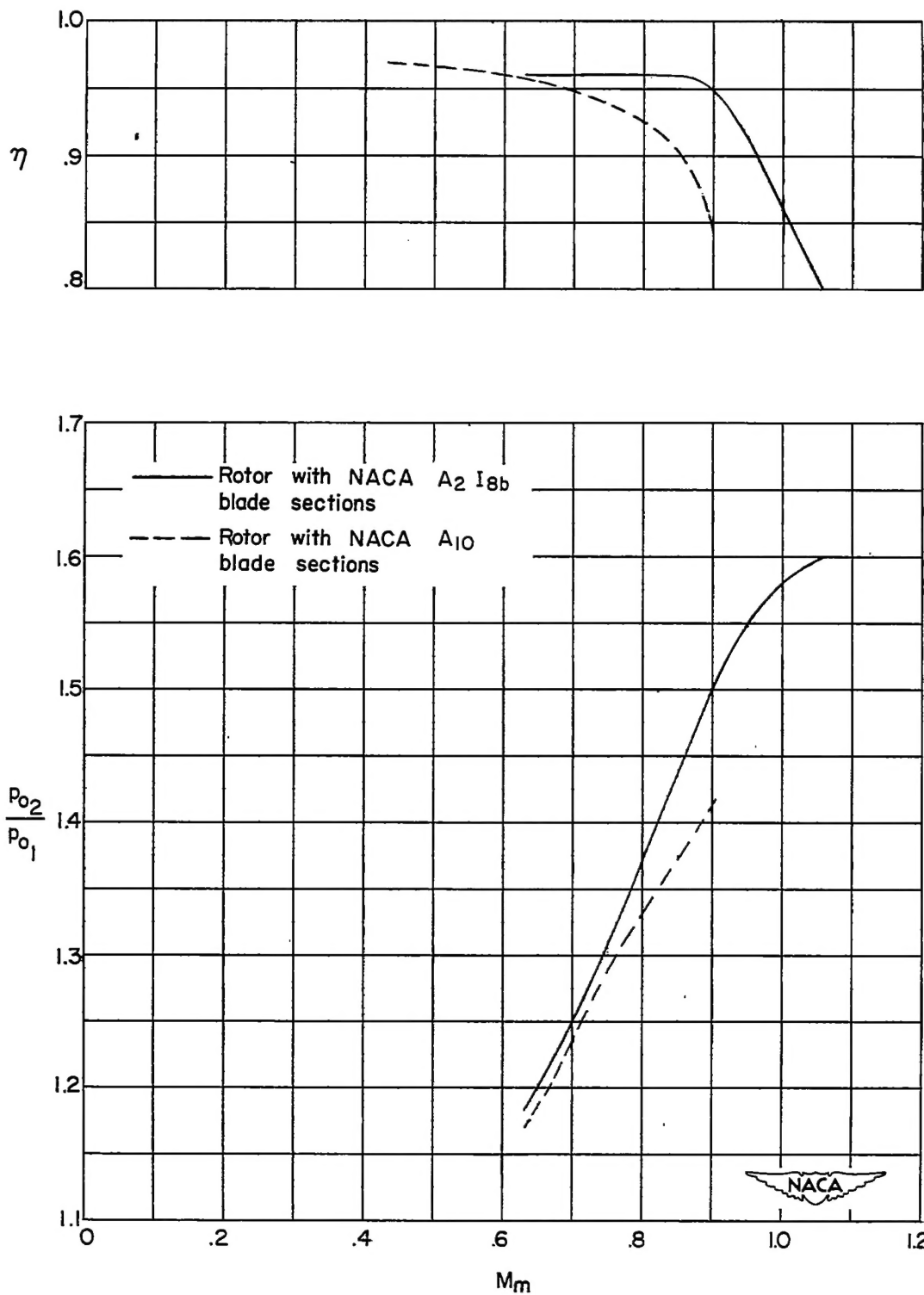


Figure 19.- Variation in peak efficiency and associated total-pressure ratio with relative inlet Mach number at mean radius.